6-4-2018 3:00 PM

# Characterization of Human Prostate Cancer Using Sodium Magnetic Resonance Imaging

Nolan Christopher Broeke
*The University of Western Ontario*

Supervisor
Scholl, Timothy J
*The University of Western Ontario*

# Abstract

Overtreatment of prostate cancer is a significant problem in the health care of men. Development of *non-invasive* imaging tools for improved characterization of prostate lesions has the potential to reduce overtreatment. In this thesis work, we will evaluate the ability of tissue sodium concentration obtained from sodium magnetic resonance imaging (sodium-MRI) to characterize *in vivo* prostate lesions. Imaging data, including multi-parametric magnetic resonance imaging (mpMRI) and sodium-MRI, were obtained from a cohort of men with biopsy-proven prostate cancer and compared to digitized whole-mount histopathology after prostatectomy. Histopathology was independently graded for Gleason score to be used as the *ground truth* of tumour aggression. These imaging data were all accurately co-registered, allowing for direct comparison of imaging contrast to Gleason score. The results of this thesis work suggest that tissue sodium concentration assessed by sodium-MRI has utility as a part of a "*non-invasive imaging-assay*" to accurately characterize prostate cancer lesions. Sodium-MRI can provide clinically useful, complementary information to mpMRI; ultimately leading to better characterization of prostate lesions throughout the whole prostate. This has potential to improve patient outcomes of men with low-risk disease who do opt for active surveillance instead of treatment.

## Keywords

# Co-Authorship Statement

This thesis contains materials which have been submitted for publication and have be presented at various conferences, including; Imaging Network of Ontario (ImNO) 2017, London Health Research Day (LHRD) 2017, Robarts Research Retreat (RRR) 2017, London Imaging Day (LID) 2017, Imaging Applications in Prostate Cancer 2017, Imaging Network of Ontario (ImNO) 2018, International Symposium on Magnetic Resonance in Medicine (ISMRM) 2018. The contributions of co-authors are listed below.

The manuscript entitled "Characterization of Clinical Human Prostate Cancer Lesions Using 3.0-T Sodium-MRI Registered to Gleason-Graded Whole-Mount Histopathology" was submitted to the *Journal of Magnetic Resonance Imaging* in May 2018. The co-authors of this manuscript are Justin Peterson, Joseph Lee, Peter Martin, Adam Farag, Jose A. Gomez, Madeleine Moussa, Mena Gaed, Joseph Chin, Stephen Pautler, Aaron Ward, Glenn Bauman, Robert Bartha, and Timothy Scholl. As the first author in the manuscript, Nolan Broeke was responsible for image registration and full data and statistical analysis, preparation of figures and manuscript drafts as well as manuscript editing. Justin Peterson and Joseph Lee assisted with registration of the first 3 data sets analyzed, Peter Martin helped with registration of the *ex vivo* and histology image sets, Adam Farag was responsible for building the custom sodium-MRI hardware which was instrumental to this research. Drs. Jose A. Gomez and Madeleine Moussa were responsible for supervising the histological Gleason grading of excised prostates, which was carried out by Dr. Mena Gaed. Drs. Joseph Chin and Stephen Pautler were the surgeons who performed the prostatectomy surgeries on patients, and Dr. Aaron Ward was responsible for design of the registration pipeline used in this research. Dr. Glenn Bauman was instrumental to this research, organizing the primary prostate imaging study and supervising

# Acknowledgments

First, would like to acknowledge my supervisor, Dr. Timothy Scholl for his guidance and support throughout my master's studies. I feel as if I couldn't express how appreciative I am for the opportunity he provided me with here at Western University. During my time as a graduate student, I am grateful for both his patience and expertise as we worked together on this thesis work. He has been so generous, providing me with funding to complete my thesis work and excellent opportunities to present my work at conferences such as the Imaging Network of Ontario, London Health Research Day, London Imaging Day, Robarts Research Retreat, Imaging Applications in Prostate Cancer Meeting, and the Cellular and Molecular Imaging Symposium. In June, I will be travelling to Paris, France to present this research at the Annual Scientific Meeting of the International Society for Magnetic Resonance in Medicine. I am very grateful for these opportunities. I am also thankful for his genuine interest in my academic success, both as his graduate student and in my future endeavors. He took the time to write numerous references letters and was always my advocate throughout my time as his master's student. While working in his lab, he provided an environment that facilitated both work and friendships, and he always showed that he cared about his students and their well-being. You were always patient to answer my questions, and sometimes gave me the opportunity to figure it out on my own, which I appreciate now as it helped me grow as a researcher. For all that you did for myself and our lab I want to say thank you very much, Tim.

I want to thank my lab members: Yonathan Araya, Alireza Akbari, Adam (Trung) Le, Patrick (Heeseung) Lim, Nivin Nystrom, Francisco Martínez-Santiesteban. Your input on the data analysis, help with learning how to use the Slicer software and the many hours of help with course assignments is something I will always value. I also thank you all for your

assistance making figures, graphs and tables, but most of all, thank you for your emotional support and company which has made my time as a graduate student memorable.

I also wanted to acknowledge other members of the CMI lab group: TD (Tian Duo) Wang, Katie Parkins, Dr. Amanda Hamilton, and Ashley Makela for being great desk-mates. I always enjoyed getting coffee together, have interesting conversations about sports or pop-culture and your help answering my many questions about how to succeed in graduate school.

I want to thank the MR technologists Dave Reese and Trevor Szekeres for all your help imaging the patients used for the analysis in this thesis work. I want to thank Adam Farag for his help with the sodium phantom imaging. I want to extend my gratitude to Justin Peterson for all his help, specifically taking the time to answer my questions about the registration pipeline and data analysis. I want to thank Cathie Crukley for preparation of the whole-mount prostate sections used for histology.

I want to thank my supportive and loving family; Mom, Dad, Scott and Nicole. Our family is the most important aspect of my life. You have all provided me with opportunities that I can never express my gratitude for. I always know that I have a source of unconditional love and support if I needed it. I always knew that you were just a Facetime call away when I was homesick and needed to hear your voices. Going all the way back to my undergraduate degree at Queens University, you have always been my outlet for support. I can never thank you all enough for providing me with the resources to go away for university, I know that is not something that most people are fortunate enough to do and I thank you dearly for that. When I was away for school, you never once mentioned that you wished I was home in Calgary more often, I understand how selfless this was of you and I wanted to say thank you and I love you all so much.

And of course, I would not be where I am without Gabrielle. I am certain that I wouldn't have gotten through my master's studies without you. I witness that each day you woke up and put yourself second. If I was busy working, you would take time out of your studying to cook meals, get groceries, and support me, never asking for anything in return. You made my time throughout my Graduate degree memorable, as we went on many fun adventures, while taking time to enjoy each other's company by going to the Gym, doing many crossword puzzles at Starbucks on the weekends, and many movie nights to name a few! You were my source of emotional support and you helped me to stay motivated to do my best throughout my master's degree. Thank you for all you do and have done Gabrielle and I am excited for a new chapter together in Calgary.

# Table of Contents

# List of Tables

# List of Figures

# List of Appendices

# List of Abbreviations

| | |
|---|---|
| $[Na^+]_{ex}$ | Extracellular sodium concentration |
| $[Na^+]_{in}$ | Intracellular sodium concentration |
| $^1H$ | Hydrogen ion |
| $^{23}Na$ | Sodium ion |
| ADC | Apparent diffusion coefficient |
| AJCC | American Joint Committee on Cancer |
| ANOVA | Analysis of variance |
| AS | Active surveillance |
| ASAP | Atypical small acinar proliferation |
| ATP | Adenosine 5'-triphosphate |
| BMI | Body-mass-index |
| BPH | Benign prostatic hyperplasia |
| cm | Centimeter |
| CZ | Central zone |
| DCE | Dynamic-contrast enhanced |
| DRE | Digital rectal exam |
| $\Delta T_2$ | Percent change in $T_2$-weighted signal intensity |
| $\Delta TSC$ | Percent change in tissue sodium concentration |
| DWI | Diffusion-weighted imaging |
| ER | Endorectal |
| ETC | Electron transport chain |

| | |
|---|---|
| FOV | Field of view |
| Gd | Gadolinium |
| GG | Gleason grade |
| GMR | Gyromagnetic ratio |
| GS | Gleason score |
| H&E | Haematoxylin and Eosin |
| Hz | Hertz |
| IGPC | Image-guided-prostate-cancer |
| mg | Milligram |
| ml | Milliliter |
| mm | Millimeter |
| mpMRI | Multi-parametric magnetic resonance imaging |
| MRI | Magnetic resonance imaging |
| ms | Milliseconds |
| NaCl | Sodium chloride |
| NADPH | Nicotinamide adenine dinucleotide phosphate |
| NCCN | National Comprehensive Cancer Network |
| ng | Nanogram |
| NHE1 | Sodium-hydrogen antiport |
| PCa | Prostate cancer |
| PET | Positron emission tomography |
| PIA | Proliferative inflammatory atrophy |
| PIN | Prostate intraepithelial neoplasia |

| | |
|---|---|
| PSA | Prostate-specific antigen |
| PSMA | Prostate-specific membrane antigen |
| PZ | Peripheral zone |
| RF | Radiofrequency |
| ROI | Region of interest |
| RP | Radical prostatectomy |
| SNR | Signal-to-noise ratio |
| T | Tesla |
| TCA | Tricarboxylic acid |
| TE | Time-to-echo |
| TNM | Tumour, Node, Metastasis |
| TORO | Transmit-only receive-only |
| TPS | Thin plate spline |
| TR | Time-to-repetition |
| TRUS | Transrectal ultrasound |
| TSC | Tissue sodium concentration |
| TURP | Transurethral resection of the prostate |
| TZ | Transitional zone |

Chapter 1

# 1    Introduction

The objective of Chapter 1 is to provide the introductory information about the work described in Chapters 2 and 3. This includes necessary information about the Prostate Gland (Section 1.1), Prostate Cancer (Section 1.2), The Sodium Ion in the Tissue Environment (Section 1.3), $^1$H Magnetic Resonance Imaging (Section 1.4), and $^{23}$Sodium Magnetic Resonance Imaging (Section 1.5).

## 1.1  The Prostate Gland

The human prostate gland is situated in the genitourinary region of the male body. This section provides background information regarding the anatomy and physiology of the human prostate gland.

### 1.1.1    Prostate Anatomy

The prostate gland is a compound tubuloalveolar gland of the male reproductive system. It is situated within the pelvic cavity, in the genitourinary region of a man's body. It is located inferior to the bladder and anterior to the rectum. It is both glandular and muscular. The young prostate weighs approximately 20 grams and is roughly the size of a golf ball (4 × 2 × 3 cm). Over time, the size of the prostate increases as men age due to benign conditions such as benign prostatic hyperplasia (BPH) or cancerous conditions such as adenocarcinoma. It consists of 70% glandular tissue and 30% fibromuscular stroma [1].

The upper portion of the prostate is called the base and it rests just inferior to the bladder; the base is adjacent to the bladder. The gland has a conical shape, making the inferior apex narrower than the superior base [2]. The urethra runs through the middle of the prostate gland, where it is called the prostatic urethra (Figure 1-1). Two ejaculatory ducts run through the prostate carrying the seminal composition of semen from the seminal vesicle into the urethra. The prostate muscles are important to ensure semen moves through the prostatic urethra and they play a minor role in ejaculation. The gland is divided into four main distinct zones: peripheral zone (PZ), central zone (CZ), transitional zone (TZ) and anterior-fibromuscular stroma (Figure 1-1).
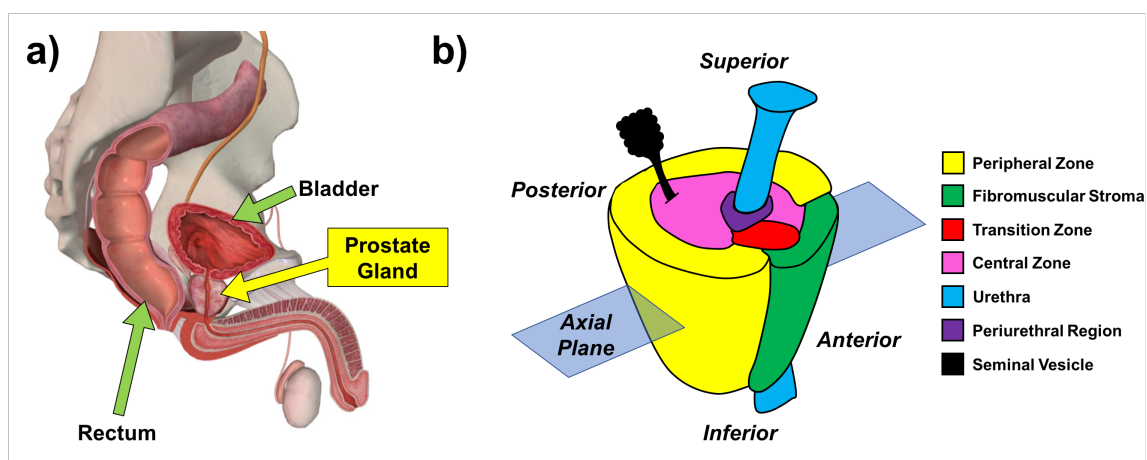


**Figure 1-1. a) Sagittal cut of the genitourinary region of the male body, illustrating the *in vivo* location of the prostate gland relative to the bladder and rectum. Image adapted from the online program, *BioDigital Human*. b) Zonal prostate gland anatomy. The major zones of the gland are identified in the diagram and legend to the right. Superior, Inferior, Anterior, and Posterior landmarks are provided for orientation. The plane of an axial image cut is also shown; this is the approximate orientation of the prostate images shown in this thesis.**

The peripheral zone is a mustache-shaped area which is the largest zone of the prostate. The peripheral zone comprises approximately three quarters of the glandular prostate tissue [1] and is the most common site of prostate inflammation (chronic prostatitis). The peripheral zone is the portion of the gland that is palpated by a physician through the rectum during a digital rectal exam (DRE). Approximately 70-80% of the prostatic cancers occur in the PZ [3]. The central zone is located within the superior-posterior portion of the gland, which surrounds the ejaculatory ducts. The CZ makes up 25% of the glandular tissue but is associated with very few adenocarcinomas (1-5%) [4]. The transitional zone surrounds a portion of the prostatic urethra; this zone is known to enlarge as men age, a condition referred to as benign prostatic hyperplasia (BPH). As this zone enlarges, urethral obstruction can occur. If growth of an adenoma becomes large enough, compression of the fibromuscular band occurs. The final zone of the prostate is the anterior-fibromuscular stroma, located in the apex. This zone consists of muscle fibers and connective tissue.

## 1.1.2  Prostate Gland Physiology

The prostate gland plays an important role in male reproduction, secreting fluids which make up a large fraction of the semen volume. Approximately one third of the total volume of semen is contributed by the prostate gland, these secretions protect and nourish sperm. The prostatic secretions consist of: the simple sugars fructose and glucose, protein-splitting enzymes, zinc, and citric acid. Altogether, the prostatic secretions are slightly acidic, this helps the sperm survive in the basic environment of the vagina. The sugars play a large role in sperm motility. They are used as a nutrition and energy source to power movement of the sperm's flagellum, allowing the sperm to "swim" to the ova and fertilize it. The

secretory action of the prostate gland is carried out by acini. Acini lumens are lined with epithelial cells, which are the producers of the prostatic fluid. Therefore, prostatic secretions are collected in acinar lumens. The lumen-bound prostatic fluid then drains via a system of ducts, eventually collecting in the prostatic urethra. Prostatic epithelial cells are classified under two categories, basal and glandular cells. Basal epithelial cells are less abundant and their role in tissue is less understood; however, one of their responsibilities is production of the cellular basement membrane. The glandular epithelial cells attach to the basal epithelial cells and are found abundantly along the acini lumen wall. They are the active secretory cells in the prostate, responsible for production of prostatic fluid found in semen. In human cells, approximately 20,000 protein-coding genes are expressed [5]; not all cells express every gene, as this is determined by tissue specification. Prostate-specific membrane antigen (PSMA) is a transmembrane, enzymatic protein that is expressed in four tissues in the body: the prostate epithelium, the kidney's proximal tubules, the brush border of the small intestine (jejunum section) and the ganglia of the nervous system. Although it is expressed in four body locations, its highest expression is within prostate tissue (roughly 100 times greater than any other tissue). Within the prostate gland, PSMA is highly specific for prostatic epithelial cells. Prostate-specific antigen (PSA) is a protein produced by both epithelial prostate epithelial cells and prostate cancer cells [6]. It isn't confined to the prostate after formation, as PSA is detectable in the blood. PSA functions to liquefy the semen, liberating the sperm to swim freely [7]. Normal levels of PSA in the seminal fluid are typically 0.5-5 mg/ml, which is a concentration $10^6$ larger than found in the blood. This is because retrograde release of PSA into the bloodstream of healthy men is not a common event; therefore, excessive escape of PSA into the blood is only facilitated by destruction

of the prostate basement membrane [7]. Normal concentrations of PSA in the blood is not well defined. Age and racial demographics can influence the range of what is considered healthy. For men below the age of 50, healthy PSA levels for Asian Americans, African Americans and Caucasians were seen to be 0 - 2.0 ng/ml, 0 - 2.0 ng/ml, 0 - 2.5 ng/ml, respectively [8]. These numbers are subject to increase with age, and this is thought to be associated with a normal, age-related, increase in prostate size.

## 1.2  Prostate Cancer

A persistent belief in our society is that "cancer" is a deadly disease that always needs to be treated as soon as possible; however, this is not always the case. Regardless, the public maintains this belief. For some types of cancer, like prostate cancer, this widespread idea has unfortunate implications. Typically, men diagnosed with prostate cancer have the option to choose either active surveillance or more radical treatment. Men facing this decision are also faced with uncertainty that is associated with living with untreated cancer. Additionally, the widespread notion that cancer is always a deadly disease can lead to men with low-risk cancer choosing treatment even if it was not necessary for them. This phenomenon is called overtreatment. In this section, we will outline current statistics regarding prostate cancer, describe the current prostate cancer grading system, outline how prostate cancer is diagnosed and describe the treatment and overtreatment of the disease in our health care system.

### 1.2.1  Prostate Cancer Statistics

One in seven men will be diagnosed with prostate cancer (PCa) in their lifetime, making it the most common malignancy in males [9]. Post-mortem studies of men who died from unrelated causes have identified that the instances of prostate cancer in deceased men was roughly proportionally to their age [10]. For example, in a random population sample of men 65 years old, approximately 65% of them would have non-aggressive PCa. In 2017, there were 103,100 new cases of cancer in Canadian men. 20.4% of those cases were prostate cancer, which was the largest share [9]. Although one in seven men are diagnosed with this malignancy, the lifetime probability of dying from prostate cancer is

just 1 in 28 men. This is much lower than the risk of death for all cancers combined, which was estimated to be 1 in 3.5 persons [9]. The overall mortality rate for PCa has been steadily declining by 3.3% every year since 2001, owing to improved treatment techniques for both early- and late-stage disease. Risk of death associated with prostate cancer has been seen to rise in men with both diabetes and higher body-mass-index (BMI) [11, 12]. The age of a man is a strong predictor of instances of new prostate cancer diagnosis. In 2017, there were 21,300 new cases of prostate cancer diagnosed on Canadian males. The age range of 30-39 was the youngest age group where new diagnosis was made, accounting for just 0.02% of all new diagnosis. The percentage of new cases in relation to age range increases monotonically with age group up to ages 60-69: 1.7% for men 40-49, 16.9% for men 50-59, 38.5% for men 60-69. The most common age group for diagnosis was men 60-69. Men aged 70-79 accounted for 29% of new diagnosis and males over the age of 80 accounted for 14% of all new PCa diagnosis. Post-diagnosis, the 5, 10 and 15-year survival rates of prostate cancer are very high: 99%, 98%, and 96%, respectively. The most common prostate malignancy is adenocarcinoma accounting for approximately 98% of all prostate cancer [13]. Adenocarcinoma originates in the epithelial gland cells, which are responsible for formation of mucus and the prostatic fluid of semen. Adenocarcinomas are most commonly found in the peripheral zone, where they are palpated during a digital rectal exam. Of the men with newly-diagnosed prostate cancer, 50% are assigned to the low-risk cancer group. Low-risk, or indolent cancer has low associate mortality and little chance of metastasis. The number of low-risk men who do choose active surveillance (AS) is increasing, as over 50% low-risk men will now opt for AS instead of treatment; however,

this number is still lower than the number of men who could be properly treated with active surveillance [14].

## 1.2.2 Grading Prostate Cancer Aggression

In 1966, Donald F. Gleason established the Gleason Scoring System. He amended his own system twice (in 1974 and 1977) [15] and had become the clinical standard for characterizing the aggression of prostate cancer until 2015. Today, grade grouping is used as the standard to stage the prostate cancer of men. Grade grouping incorporates a patients Gleason score to separate men into one of five categories that designate increasing levels of aggression. The Gleason scoring system is based on low-power, microscopic observation of the morphological features in prostatic tissue samples. Specimens sent for grading are obtained from either needle-biopsy as tissue cores, or whole prostate gland sections obtained after radical prostatectomy. Tumour cells are then judged to fit within five distinct categories, called Gleason grades. These grades range from 1 to 5 and represent different states of complexity in morphology. Grade 1 is the least aggressive on the scale and grade 5 is the most aggressive. Figure 1-2 illustrates the cellular and tissue morphology seen with varying Gleason grades, visualized with histology. Within an identified lesion, the most prevalent tumour grade is denoted as the primary grade and the second most prominent grade of lesion in an area becomes the secondary grade. Gleason score (GS) is a combination of the primary and secondary Gleason grades (GG): Gleason Score = primary grade + secondary grade.
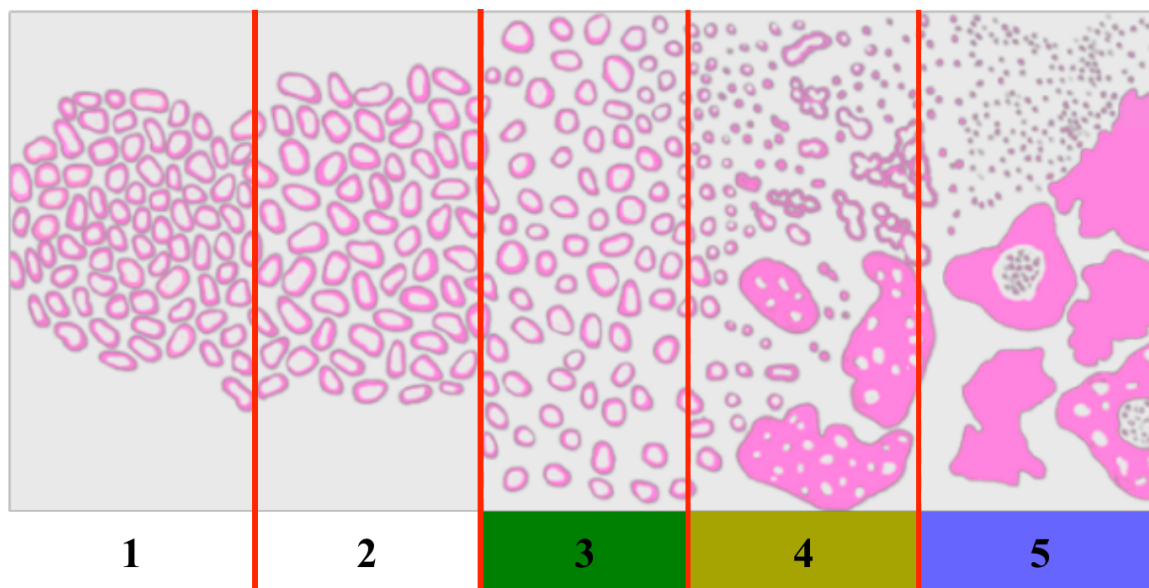
**Figure 1-2. Cellular and tissue characteristics of Gleason grades 1-5 are shown in panels from left to right (1-5). On the Gleason Grading System, Grade 1 is the lowest classification. It is assigned to tumour tissue which is determined to be the least aggressive. Tumour aggression increases monotonically with Gleason grade until grade 5. Grade 5 is the highest grade given in this grading system. At grade 4 (see panel 4), cribriform structures become present in the tissue (larger, pink-filled structures on the bottom of the grade 4 panel). This figure is adapted from an image in an article published by Epstein *et al.* (2005) [16].**

The lowest grades of cancer on the Gleason grade scale are grades 1 and 2. Combinations of these grades result in GS 2-4 (Gleason 1+1, Gleason 1+2, Gleason 2+1, and Gleason 2+2), which are rarely diagnosed. This is because the accuracy and utility of giving this assessment is debated. Cores extracted from needle biopsy and assigned Gleason scores of 2-4 often represent an under-grading of more aggressive lesions [17]. Previous studies showed that 55% of needle biopsies, graded with Gleason scores 2-4,

showed extra-prostatic extensions after radical prostatectomy [18]. Other research has associated a very low-risk of patient death within 15 years of Gleason score 2-4 diagnosis [19]. However, these tumours were obtained through transurethral resection of the prostate (TURP). Low-volume Gleason score 2-4 tumours found using TURP are often indolent compared to tumours taken from needle biopsy. In addition, reproducibility of the GS 2-4 diagnosis by urological pathologists is low [17, 20]. The uncertainty associated with GS 2-4 is problematic for patients who are assigned this score, as this grade of cancer has a low chance of progression and therefore patients possessing it are not sent for treatment [17]. If we are going to steer patients away from treatment in our healthcare system, we need to be very confident that GS 2-4 lesions are not under-grading of more aggressive cancer. Therefore, literature has suggested that there is little risk to patients to instead assign GS 2-4 cancer with a Gleason score of 5 or 6. By doing this, we will be decreasing the chances of misdiagnosing higher stage foci. Gleason grade 3 from biopsy is a reliable determination and is the most common Gleason pattern identified on biopsy cores. In GG 3 (Figure 1-2, category 3), cells are smaller than GG 1 and 2 and infiltration between benign glands is a common characteristic. Importantly, grade 3 gland cells still have a distinguished border. Gleason grade 4 is identified as poorly-formed or fused gland cells [21]. Further, at GG 4, cribriform gland adenocarcinomas are present. All cribriform adenocarcinomas are classified as $\geq$ GG 4 [22]. These structures have been seen to be strong predictors of metastasis in patients with Gleason score 7 cancer at radical prostatectomy [23]. Cribriform structures are identified on histology as having a sieve-like appearance. Prostate cells with this cribriform structure have irregular edges and an unrecognizable lumen (Figure 1-2, category 4). Gleason grade 4 cells are often fused together, with no stroma separating the

cells. Gleason grade 5 is the highest (most aggressive) grade of cancer than can be assigned in the Gleason system. Gleason grade 5 tissue has limited gland formation and does not resemble normal prostate tissue. Common patterns seen in GG 5 include planar sheet of tumour, individual cells, and long cords of cells [21]. Comedonecrosis is defined as necrotic tissue in the luminal space. This is an uncommon tissue characteristic but, when present, is classified as GG 5. Often, Gleason grade 5 is an under-graded cell type [24]. Not shown in Figure 1-2 are the "precancerous conditions" of the prostate, including: prostatic intraepithelial neoplasia (PIN) and proliferative inflammatory atrophy (PIA) and benign prostatic conditions such as: BPH and atypical small acinar proliferation (ASAP). PIN is defined as an abnormal condition of the epithelial cells which line the acini. Since adenocarcinomas arise from epithelial cells and make up approximately 98% of all prostate cancers, PIN is identified as a potential precursor to malignancy. Histologically, they present with prominent nuclei in an existing duct structure. BPH is a non-cancerous enlargement of the prostate that is a result of the second phase of prostate growth that begins when men are over 25 years of age. This enlargement squeezes the prostatic urethra and creates many secondary effects that affect patient quality of life. BPH often presents with lower urinary tract symptoms [25]. These symptoms are categorized as either voiding symptoms: weak urine stream and incomplete bladder emptying, or storage symptoms: frequent need to urinate leading to nocturia [26]. The instances of BPH are high, affecting 50% of men by the time they are 60 [26]. Atypical small acinar proliferation (ASAP) is an abnormal growth of gland cells in the prostate. ASAP that is suspicious for malignancy will be identified as groups of cells that are highly suggestive of cancer but are not diagnostic for carcinoma [27]. ASAP suspicious for malignancy that is discovered after

core biopsy is highly predictive of subsequent adenocarcinoma on repeat biopsy. Proliferative inflammatory atrophy (PIA) are identified as frequently occurring, atrophic prostate lesions. Studies have identified the imbalance between proliferation and apoptosis in PIA cells [28] which supports its connection with carcinoma. It is a benign lesion with potential to degenerate into PIN or carcinoma. PIN, ASAP, and PIA are identified as pre-cancerous conditions, but some experts do not think that they necessarily are linked to increased risk of developing prostate cancer, therefore men with these cell types are not treated.

## 1.2.3 Prostate Cancer Diagnosis

The National Comprehensive Cancer Network's (NCCN) guidelines stipulate that asymptomatic men can be classified as having suspected prostate cancer after an abnormal digital rectal exam (DRE). A digital rectal exam is performed by palpating the peripheral zone of the prostate, to estimate its enlargement. In the early 1900's DRE screening lead to improvement of PCa patient staging and thereafter was recommended as an annual procedure for men over 50 [29]. However, the nature of the exam is uncomfortable for the patient and depends on a subjective, skill-dependent evaluation by the physician about the size and stiffness of the gland. Presently, DRE is used in conjunction with other tools to aid in diagnosis of prostate cancer. One of these tools is the PSA blood test, which has been seen to help detect prostate cancer. In previous study, 33% of men with PSA levels above 4 ng/ml were seen to have biopsy detected malignancy [30]. The lack of specificity that high PSA levels has for prostate cancer is likely do to unforeseen PSA-elevating circumstances such as BPH, prostate manipulation during a DRE and/or biopsy, and

prostatitis [31]. Another diagnosis technique that is employed after a patient presents in the clinic with a suspicious DRE and elevated blood PSA levels is a 2D transrectal ultrasound (TRUS)-guided biopsy. The TRUS-guided biopsy is the clinical standard for prostate cancer diagnosis. In this technique, 12 needles are directed into the prostate gland on trajectories that are guided by an ultrasound probe. These needles extract tissue cores, which are subsequently pathologically examined for Gleason grade [32]. Based on the Gleason scores given, a treatment recommendation is made for patients. However, the Gleason graded biopsy tissue often miss-characterizes the stage of lesions, either through over- or under-estimation [33]. This can been attributed in part to tangential sectioning, where the needles used for tissue extraction alter the integrity of the cells sampled in the cores, leading to an incorrect determination of cell grade [34]. Additionally, the nature of biopsy technique samples less than 0.5% of the entire prostate gland, leading to high false-negative rates (21-47%), which often results in repeated biopsy [35]. In addition to Gleason score, prostate cancer can be staged by a TNM classification system [13]. This is a method adapted from the American Joint Committee on Cancer (AJCC), where each letter classification (T, N and M) denotes a location of disease metastasis. Each letter group has sub-classifications which describe the extent of cancer growth in that location. The T-category refers to the tumour within the prostate gland, and its sub-classification describes the size and extent of the primary tumour [13]. The N-category reflects the state of any regional lymph nodes. Specifically, whether cancer cells have spread to the hypogastric, obturator, internal iliac, external iliac, and sacral lymph nodes [13]. The M-category identifies any metastases to distant sites in the body. The most common sites of metastases are the bone, lymph nodes, lungs and liver [13]. The specific lymph nodes which most

commonly harbour metastases are the para-aortic, common iliac, inguinal, supraclavicular, scalene, and cervical. Table 1 below describes the subcategories of each classification.

**Table 1-1. TNM classification of prostate cancer. Table adapted from the classifications outlined in National Comprehensive Cancer Network Guidelines for Patients, Prostate Cancer, Version 1.2016 [13].**

| | | |
|---|---|---|
| **T-Category** | T1 | Any tumours cannot be felt by DRE or seen with imaging. These tumour types are diagnosed with abnormal blood PSA levels. |
| | T2 | Tumours can be felt by a physician during DRE and are visible with imaging. T2 score defines growth of tumour cells that are confined to prostate gland. |
| | T3 | Tumour cells are present beyond the prostate gland. Cells have reached surrounding connective tissue, seminal vesicles or the neck of the bladder. |
| | T4 | Tumour cells have invaded other tissue types and may be fixed onto these other tissues. Nearby tissue includes: rectum, bladder, external sphincter, pelvic wall, and surrounding muscles. |
| **N-Category** | NX | It is unknown if cancer has spread to lymph nodes. |
| | N0 | No cancer found in nearby lymph nodes. |
| | N1 | Cancer has spread to nearby lymph nodes. |
| **M-Category** | MX | No knowledge if cancer has spread to distant sites. |
| | M0 | No cancer growth in distant sites. |
| | M1 | Tumour cells have invaded distant sites. |

## 1.2.4    Prostate Cancer Treatment and Overtreatment

For patients diagnosed with prostate cancer, many different treatment options are available to these men. A panel review in 1995 by the American Urological Association outlined that patient preferences should guide treatment decision making [36]. This decision is difficult for patients, as men are given the option to choose either active surveillance (AS) or immediate, more invasive treatment interventions. Active surveillance is an observational strategy that allows patients to delay, or possibly avoid altogether, therapeutic treatment measures. This is done without threatening the patients long-term cancer-specific survival [37, 38]. Commonly, patients recommended for AS have been characterized to have lower-risk, or clinically insignificant, PCa in biopsy cores. Clinically insignificant disease is defined as limited volumes of cancer, characterized as Gleason score $\leq$ 6, found on less than 3 of the 12 cores extracted. Additionally, this cancer must have less than 50% involvement in any of the 12 cores. In AS, men visit their physician for bi-annual (every 6 months) PSA blood tests and an annual DRE. Additionally, biopsy is performed on these patients every 12 months to help further characterize the stage of the lesions. In some healthcare systems, depending on the country each man lives in and access to resources based on region of residence, multi-parametric-MRI (mpMRI) examinations are included in AS protocols. There is concern with this technique, as it has been suggested that AS only delays the inevitable (radical intervention) and potentially results in patients missing the therapeutic window for curing their disease. Therefore, men who are expected to live more than 20 years post-diagnosis often may choose therapy regardless. This is because within their life-expectancy time frame, their cancer may metastasize outside the prostate. The lifetime costs of AS of prostate cancer, identified through a Canadian

Healthcare associated costs assessment are approximately $18,500, including potential delayed treatment [39]. It is estimated that active surveillance results in approximately 12.5 quality-of-life adjusted years for men who chose this option [39]. If men do choose immediate intervention instead of active surveillance, radical prostatectomy (RP) is the most frequently given prostate cancer treatment. Radical prostatectomy is a surgical procedure that removes the whole prostate gland, seminal vesicles, and vas deferens [37]. There are different types of RP, including nerve-sparing and non-nerve-sparing. The choice between these two techniques is largely dependent on the patient's sexual function and the characteristics of the cancer. As well, nerve sparing surgery has been seen to lower instances of incontinence post-surgery. This procedure has obvious benefit to men with stage T1 and T2 prostate cancer (tumour cells that are totally confined to the gland) as removal of the gland ensures total elimination of the cancer. Another possible procedure for men with PCa is interstitial prostate brachytherapy and external beam radiation therapy. Brachytherapy treatment involves radiation where the radioactive source is within the prostate gland. This can be in the form of radioactive seeds (low-dose radiation) or through needles inserted into the prostate gland (high-dose radiation). External beam radiation therapy is another option for men, with certain techniques such as intensity modulated radiation therapy (IMRT) and volumetric modulated arc therapy (VMAT) being used to maximize cancer cell radiation while limiting healthy tissue exposure. For men who choose radical treatment, the estimated healthcare-associated costs have been calculated to range from $24,000 to $30,000 depending on the type of treatment given [39]. Further, these men enjoyed approximately 11 years of quality-of-life adjusted years, which was 1.5 years less than AS [39]. For men who underwent prostatectomy, studies have identified that at three

years post-surgery, over 90% of these men experienced sexual dysfunction and over 50% of them dealt with some level of incontinence [40].

Due to the persistent notion in our society that all cancer is lethal and must be treated, there is a large psychological burden that is associated with men choosing active surveillance over radical treatment. This leads to conservative decision making by both clinicians and their patients about the optimal way to treat each man's cancer. Overdiagnosis is defined as patients receiving further treatment interventions, such as radical prostatectomy, and brachytherapy, who would be more appropriately treated with active surveillance. Up to 80% of men who are screened with the PSA blood test, and are detected to have prostate cancer, are over-diagnosed and subsequently overtreated [41]. Improved patient acceptance of AS protocols is one of the ways to combat this problem. Accurate characterization of low- and high-risk prostate cancer can reduce overtreatment of men with low-risk disease. It is estimated that improved compliance of patients for AS would save the Canadian health care system $100 million per annual cohort of men diagnosed with PCa. On a per patient basis, AS saves anywhere from $6,000 to $12,000 compared to treatment, while providing more quality-of-life adjusted years for patients [39]. It stands to reason that better imaging tools for lesion characterization throughout the entire gland would improve risk stratification. This in turn, would bolster patient and physician confidence in surveillance, reducing overtreatment of this disease.

## 1.3  The Sodium Ion and Tumour Metabolism

This section provides background information about the process and transporters involved in sodium ion flux in cells. Additionally, it will touch on the metabolic processes of both healthy tissue and cancer cells. These pathways have downstream effects on the concentration of sodium ions in the tumour cell environment.

### 1.3.1   Sodium Ion Flux in Cells

The sodium ion is involved in many active cellular processes in the body including: muscular contraction and conduction of nerve impulses. In tissue, there are two different sites where sodium ions can reside: the intracellular space and the extracellular matrix. The sodium-hydrogen ($Na^+/H^+$) antiport (NHE1) is a membrane-bound protein which is involved in sodium movement across the cell membrane. This exchanger influxes sodium ions into cells, and its activity is balanced by a sodium-potassium ($Na^+/K^+$) ATPase activity, which drives sodium ion efflux into the extracellular matrix. These transporters help cells maintain sodium homeostasis. NHE1 exchanges an intracellular $H^+$ ion for an extracellular $Na^+$ ion with a 1:1 ratio. This exchange is driven by cells' innate need to maintain an optimal intracellular hydrogen ion concentration. When this concentration fluctuates too high or too low, stresses are felt by the cell. Specifically, this influences the intracellular pH. Therefore, cells have adapted efficient mechanisms to control the intracellular $H^+$ ion concentration. The sodium-hydrogen antiporters are found in abundance across the cytoplasmic membranes of eukaryotic cells and the intracellular organelles. The function of NHE1 is regulated by sensitive indicators that sense when the cell requires its activity. Tissue sodium concentration (TSC) is a weighted average of the

intra- and extracellular sodium ion concentrations in tissue. This weighted average is based upon the relative compartmental sizes (volume) of the intracellular space and extracellular matrix. Since sodium is a common product of cellular processes, TSC measurements are likely to be sensitive indicators of changes in cellular function linked to disease.

## 1.3.2    Metabolic Activity in Healthy and Tumour Cells

Humans are multicellular organisms that are made up of highly evolved cells. These cells compose tissues and have adapted very complex signaling pathways which allow us to exist, grow, heal, and reproduce. One of these complex pathways is the regulation of metabolism. For cells, there are two main types of metabolism. When stimulated by growth factors, cells will undergo proliferative metabolism and focus on generating cellular biomass which includes carbon, nitrogen, and excess energy. These cellular biomass materials are the building blocks needed to divide and reproduce a new, viable cell. However, most of the time, cells are not stimulated by growth factors, and therefore they undertake differentiated cell metabolism. In full, differentiated metabolism turns sugar molecules (glucose), into cellular energy (adenosine 5'-triphosphate (ATP)), to support the cell's energetic needs to perform its function in tissue. The first steps of this process involve cytoplasmic glycolysis. This can be done with or without the presence of oxygen (aerobic and anaerobic conditions, respectively). For each glucose molecule undergoing glycolysis, two pyruvate molecules, two protons ($H^+$), two ATP are produced. After this, the products of glycolysis are pushed into one of two metabolic sub-categories based on the availability of oxygen in the tissue environment. When oxygen is present in healthy tissue, pyruvate is shunted into the mitochondria for admittance into the tricarboxylic acid (TCA) cycle (this

is also known as the Krebs or Citric acid cycle). After this, the TCA cycle products are sent to the electron transport chain (ETC), where ATP is produced with very high yield (~ 36 mol ATP/mol glucose). This pathway maximizes energy output per glucose molecule, while also minimizing the production of lactate. This whole pathway is collectively known as oxidative phosphorylation. In anaerobic conditions, the cells proceed with repeated glycolysis, a pathway which has a much lower ATP yield per sugar molecule (~ 2 mol ATP/mol glucose).

There are significant differences in the production of energy in tumour cells compared with healthy cells. Tumour cells often rely on increased rates of glycolysis for energy production regardless of the presence of oxygen, in what has been called "aerobic glycolysis" [42]. More commonly, these whole-scale metabolic changes in tumour tissue are referred to as the Warburg Effect. The phenomenon was first described by Dr. Otto Heinrich Warburg in 1924 [43]. He originally hypothesized that defective mitochondria caused this altered metabolism [44]; however, future work has suggested that this is not the case and that other factors may be the cause [45]. It should be noted that aerobic glycolysis is often a common pathway for healthy cells when they are exposed to scarce resources. However, tumour tissue is not commonly found in such environments. Instead, tumour tissue eschews the efficient energy production of oxidative phosphorylation to ensure that they accumulate the necessary biomass required for proliferation. The reason for this is that for proliferation, cells have metabolic needs that extend well beyond high ATP levels; to produce viable daughter cells, the parent must accumulate biomass such as nucleotides, amino acids, and lipids. Synthesis of amino acids and nucleotide requires catabolism of reduced nicotinamide adenine dinucleotide phosphate (NADPH) and carbon

molecules, making production of excess ATP less of a concern for these cells. A glucose molecule, when broken down with oxidative phosphorylation produces approximately 36 ATP as noted above. However, the same glucose molecule can also be broken down via aerobic glycolysis to form 2 ATP and 2 NADPH, which are then used for amino acid synthesis. Additionally, glucose can be used as the carbon backbone in macromolecule synthesis [42]. This highlights why the bulk concentration of glucose in proliferative tumour cells are not streamlined for oxidative phosphorylation but instead are broken down through aerobic glycolysis.

## 1.3.3   Implications on Tissue Sodium Concentration

Repeated aerobic glycolysis seen in tumour tissue leads to an increased lactate concentration within cells. This reduces the intracellular pH within tumour cells, which would normally lead to cell apoptosis. However, tumour cells avoid this outcome through increased efflux of intracellular hydrogen ions. One of the ion-transport mechanisms employed is sodium-hydrogen antiport (NHE1), mentioned above. This exchanger, which pumps out intracellular hydrogen ions for extracellular sodium ions ($[Na^+]_{ex}$), increases the intracellular sodium concentration ($[Na^+]_{in}$). Since $[Na^+]_{ex}$ is kept relatively constant through tissue perfusion [46], increased $[Na^+]_{in}$ leads to an overall increase in tissue sodium concentration (TSC). Additionally, it has been seen that intracellular acidification, as seen in tumour tissue undergoing aerobic glycolysis, increases the cell membrane concentration of NHE1 antiporters [47, 48]. This further facilitates increased $[Na^+]_{in}$ in cancer cells. Movement of hydrogen ions into the extracellular space also has supplementary benefits for the cancer tissue. Extracellular acidification contributes to degradation of the

extracellular matrix, making room for expansion of the tumour tissue [49]. Increased intracellular sodium concentration has been seen to be a good measure of cell malignancy and motility [47, 50]. TSC has been measured and compared to normal tissue in previous studies of brain and breast cancer [51, 52]. These studies identified that cancer cells exhibited a 50% increase in TSC. Additionally, low-grade Glioma has previously been observed to exhibit a 100% increase in TSC when compared to healthy tissue [53]. Therefore, TSC may have utility to characterize prostate cancer stage, allowing for better clinical decisions about patient treatment stratification based on lesion aggression.

# 1.4 Introduction to $^1$H Magnetic Resonance Imaging

In this section, general background information is provided for standard magnetic resonance imaging (MRI) of the hydrogen nuclei associated with water molecules. Information will be provided about magnetization, nuclear spin, RF pulses, longitudinal and transverse relaxation, gradient-echo sequences, $T_1$- and $T_2$-weighted imaging, and multi-parametric MRI. Further detailed explanation of these topics can be found in several references [54, 55].

MRI is a clinical diagnostic imaging modality that is known for production of images with unrivaled soft tissue contrast. It has the capability to produce three-dimensional imaging volumes that are extremely helpful for detection and differentiation of tissue structures and changes in tissue associated with disease. MRI involves the use of a strong homogenous magnetic field generated by superconducting magnets. The superconducting magnet requires liquid helium as a cryogenic cooling fluid. MRI machines can vary in field strength, and different magnet strengths are useful for both clinical and research applications. The magnetic field strength of MR systems is quantified by the SI unit, Tesla (T). Clinical MRI machines vary in the magnetic field strength, from low-field systems (0.2 T) to high-field systems (7 T) but the most ubiquitous field strengths in the clinic are 1.5 and 3.0 T.

## 1.4.1 Nuclear Spins, Net Magnetization and RF Pulses

In standard MRI, the interaction between magnetic dipole moment of protons ($^1$H) and their environment is exploited to produce images. When these dipoles are in a

magnetic-field-free environment, their orientation is random. However, when an external magnetic field, $B_0$, is applied, the nuclear magnetic dipole moments precess around the field at a frequency known as the Larmor frequency ($\omega_0$). The Larmor equation is used to calculate the Larmor frequency and is given by Equation 1.1:

$$\omega_0 = 2\pi\gamma B_0.$$  Equation 1.1

In Equation 1.1, $\gamma$ is the gyromagnetic ratio (GMR). This is an intrinsic nuclear property, measured in units of Hertz (Hz) per Tesla. For protons associated with water molecules, the GMR is $42.576 \times 10^6$ Hz T$^{-1}$. GMR is related to the strength of the magnetic dipole moment of a nucleus. At rest, the distribution of magnetic dipoles in a sample are orientated randomly, resulting in no net magnetization. However, when the volume to be imaged is placed in the external magnetic field, the distribution of precessing dipoles will have a "tendency" to align with $B_0$ and therefore the sample's dipoles will possess an overall net alignment, or magnetization. This net magnetization is called $\vec{M}_0$ (Equation 1.2) and will be aligned in the direction of the magnetic field. In MRI, it is standard practice to orient the $z$-axis of a Cartesian coordinate system along the direction of the main magnetic field. The sample magnetization, $M_0\hat{z}$, is given by

$$\vec{M}_0 = M_0\hat{z} = \frac{\rho_0\gamma^2\hbar^2}{4kT}B_0\hat{z}.$$  Equation 1.2

In Equation 1.2, $\rho_0$ is defined as the number of protons per volume, $\hbar$ designates the reduced Planck's constant ($h/2\pi$), $k$ is the Boltzmann constant and $T$ is the temperature of the sample. The magnetization that is achievable at body temperature and clinical field strength is small; this is a limiting factor in achieving high signal-to-noise ratio (SNR) in MRI. The

human body concentration of hydrogen atoms in tissue is high, approximately 88 mol/L. This helps facilitate *in vivo* imaging with protons. When we wish to detect the sample magnetization, we first "tip" the net magnetization, $\vec{M_0}$, away from its thermal equilibrium position along $B_0$ (Figure 1-2).
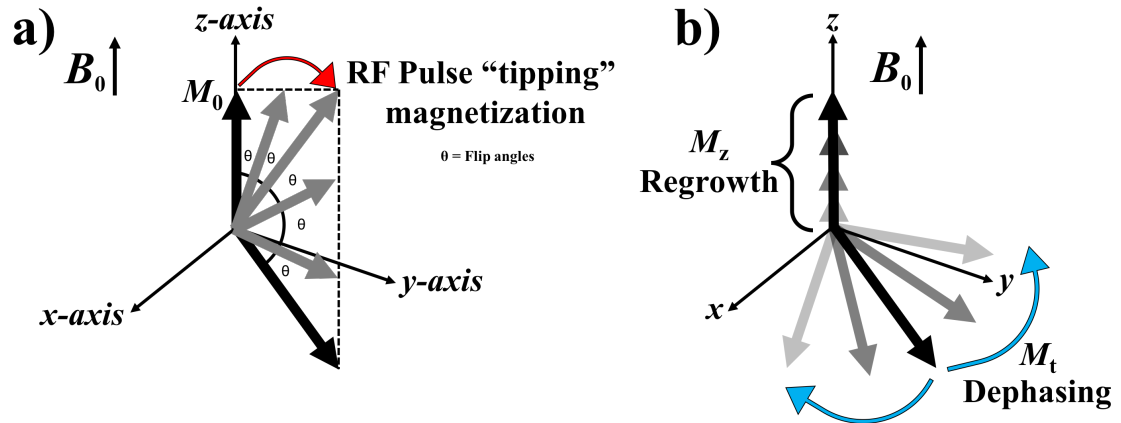


**Figure 1-3. a) Net magnetization ($\vec{M_0}$) is tipped away from the z-axis to an angle $\theta$ by a RF pulse. b) Relaxation of both transverse ($M_t$) and longitudinal ($M_z$) magnetization. Transverse magnetization dephases to zero in the *xy* plane, governed by the time constant $T_2$. Longitudinal magnetization regrows along the z-axis, governed by the time constant $T_1$.**

 "Tipping" magnetization means to perturb it away from its equilibrium position, using a transverse radio-frequency (RF) magnetic field. The transverse RF field is designated as $B_1$ and it oscillates at the Larmor frequency of the nuclei we wish to perturb. The RF field is produced by an RF transmit coil. This RF field excites the net magnetization so that it begins precession around the *z*-axis, at a specific angle $\theta$, called the flip angle (Figure 1-

2). For example, if we were to apply a flip angle of 90° (Figure 1-2a), the $\vec{M}_0$ would be excited entirely into the *xy* plane, where it would precess at the Larmor frequency.

## 1.4.2    Transverse Magnetization and Relaxation Time, $T_2$

After an RF pulse perturbs the magnetization into the *xy* plane, we create transverse magnetization, $\vec{M}_t$ (Figure 1-2b). Transverse magnetization can be further broken down into $M_x$ and $M_y$ components, given by Equation 1.3.

$$\vec{M}_t(t) = M_x(t)\hat{x} + M_y(t)\hat{y}.$$                Equation 1.3

The decay of this transverse magnetization to zero is governed by the transverse relaxation time, $T_2$. This decay of transverse magnetization is due to the interactions between the spins. Their interactions result in a distribution of spins which precess at slightly different frequencies, which eventually dephase causing decay of the net $\vec{M}_t$ to zero (Figure 1-2b). Equation 1.4 describes the decay of $M_t$ with time, governed by the time constant $T_2$.

$$\vec{M}_t(t) = M_t(t)e^{-t/T_2}.$$                Equation 1.4

Dephasing of spins is additionally increased by the effects of inhomogeneities in the local magnetic field. Field inhomogeneities can also be attributed to external sources such as imperfect magnetic field shimming or magnetic susceptibility of certain tissues in comparison to empty space (air). This is characterized by the effective spin-spin relaxation time constant of tissues, designated as $T_2^*$. $T_2^*$ is always shorter than $T_2$.

### 1.4.3  Longitudinal Magnetization and Relaxation Time, $T_1$

Longitudinal magnetization, $\vec{M}_z$, is described as the net magnetization that aligns with the main magnetic field along the z-axis. This magnetization is parallel to $B_0$ and is known as the thermal equilibrium magnetization. After an RF pulse, the resulting tipping of magnetization to the $xy$ plane reduces the initial longitudinal magnetization. The exponential regrowth of $\vec{M}_z$ is described by a longitudinal relaxation time constant, $T_1$. The $T_1$ relaxation or spin-lattice relaxation time describes the loss of absorbed RF energy to the environment around the spin system, also known as the lattice. Hence the name, spin-lattice relaxation time. $T_1$ relaxation time is always longer than the $T_2$ relaxation time for a given tissue type. Equation 1.5 describes the exponential, asymptotic regrowth of longitudinal magnetization, governed by the $T_1$ time constant:

$$\vec{M}_z = M_0\left(1 - e^{-t/T_1}\right). \qquad\qquad \text{Equation 1.5}$$

### 1.4.4  MRI Signal Detection and RF Transmission

Signal in magnetic resonance imaging is a very important aspect of good imaging. Signal-to-noise ratio allows us to quantify the quality of our imaging signal in relation to noise level. Achievable SNR varies based on the nuclei we are imaging. Low SNR can be an issue when physical limitations arise due to nuclei-dependent properties such as natural abundance and *in vivo* concentration in tissue. However, we can improve SNR by increasing the external magnetic field strength. This will increase the Larmor frequency for excitation and detection and the amplitude of longitudinal magnetization (Equation 1.1 and Equation 1.2, respectively). Signal in MRI describes the detection of RF energy that is

emitted by nuclei that was excited by the RF excitation pulse. RF transmit coils are tuned to resonate at the Larmor frequency of the nuclei we wish to image and connected to an appropriate RF source. After excitation, the transverse magnetization is detected by an induced voltage at the Larmor frequency in the receive RF coil (or the same RF coil used for excitation). Detected signal in MRI drops off very rapidly as the distance between the tissue of interest and the detection RF coil increases. Therefore, these coils are typically built to be positioned as close as possible to the volume of interest.

## 1.4.5    Gradient-echo sequences

Efficient use of transverse magnetization is key to produce images with high SNR. To optimize usage of this magnetization, the dephased spins are refocused using an "echo". In gradient-echo sequences, rephasing of dephased transverse magnetization is induced by applying a refocusing magnetic gradient pulse during standard transverse magnetization decay. This can be done multiple times, producing multiple "echoes" per RF excitation. The time between excitation of the magnetization using the RF pulse and formation of the echo is called the time-to-echo (TE) while the time between each RF excitation pulse is the time-to-repetition (TR). Gradient-echo sequences and spin-echo sequences (using RF refocussing instead of gradient refocusing) are the most frequently used pulse sequences in MR because of their versatility and simplicity.

## 1.4.6    $T_1$-weighted and $T_2$-weighted imaging

$T_1$ and $T_2$ values are inherent properties of tissues, which we can use to enhance image contrast between different tissues. By selecting a pulse sequence, such as a spin-

echo or gradient-echo, imaging data can be acquired with a $T_1$- or $T_2$-weighting. $T_1$-weighting is achieved by choosing imaging parameters to have a short TE and TR values on the order of the $T_1$ value of the tissue of interest. Contrast on $T_1$ images can be enhanced by addition of a paramagnetic contrast agent, such as chelated gadolinium. The effect on image quality seen by contrast agents owes to the fact that they increase the rate of spin-lattice relaxation of protons in surrounding tissue allowing for increased local signal in a $T_1$-weighted image. $T_2$-weighting is achieved by specifying imaging parameters to have a TE on the order of the $T_2$ value of the tissue and a long TR. In $T_2$-weighted imaging, fluids appear brighter within the images. This is because fluids have longer $T_2$ values than tissues, leading to increased signal.

## 1.4.7 Multi-parametric Magnetic Resonance Imaging

Multi-parametric magnetic resonance imaging (mpMRI) is seeing increased frequency of use in the clinic. This suite of MR imaging contrasts may include acquisition of some or all of: $T_1$- and $T_2$-weighted imaging, diffusion weighted imaging (DWI), and dynamic contrast-enhanced (DCE) imaging.

Diffusion weighted imaging is an imaging technique based on measurement of random Brownian water diffusion in tissues [56]. This motion is isotropic and is driven by thermal energy of water molecules. Signal in these images is measured from four sources, with diffusion of water existing in the extracellular space being the major contributor. The speed at which water molecules diffuse is primarily influenced by the ratio of the cellular volume (how many cells occupy a given area) and the volume of the extracellular space. Diffusion weighted images are inherently $T_2$-weighted. Apparent diffusion coefficient

(ADC) values, units of mm$^2$/second, can be calculated from DW images using Equation 1.6.

$$ADC = \frac{1}{b} \ln \frac{S}{S_0}.$$  Equation 1.6

Here, *b*-values describe the strength and timing of the gradients used to generate these images, $S$ and $S_0$ are the signal intensities at specific $b$ values chosen based on the tissue being imaged. Approximately 35% of all clinical MRI examinations are acquired using a contrast agent [57]. Contrast agents are pharmaceutical drugs that affect the magnetic environment of protons in the vicinity where they are taken up. Paramagnetic contrast agents, such as gadolinium (Gd), accelerates the $T_1$ relaxation of nearby tissue, resulting in positive signal enhancement. Superparamagnetic contrast agents such as iron oxide, predominantly increase $T_2$ relaxation rates, which leads to negative signal enhancement [58]. These contrast agents can be engineered for selective binding to a specific disease or protein producing specific and significant signal enhancement for that target [57].

In the detection of prostate cancer, sensitivity and specificity of $T_2$-weighted imaging for detection of prostate cancer has been seen to be 62% and 77%, respectively. Diffusion weighted imaging has been measured to have a sensitivity and specificity of 69% and 89%, respectively. Previous works have demonstrated that dynamic contrast enhanced imaging had a sensitivity and specificity of 43-53% and 83%, respectively. When combining $T_2$-weighted imaging, DWI, and DCE-MRI, pooled sensitivity and specificity resulted in 74% and 88%, respectively [59].

# 1.5        Sodium Magnetic Resonance Imaging

Over the past 20 years, imaging research has investigated many cellular metabolites and nuclei such as sodium as endogenous imaging biomarkers allowing for earlier detection of disease states, including cancer [51, 53, 60]. In section 1.3, detailed explanation about the flux of sodium ions in both healthy and tumour tissue has been discussed. This highlights the importance of sodium detection and use of sodium imaging in the clinical setting as it has been seen to be a biomarker of proliferation in cancerous cells. However, sodium magnetic resonance imaging (sodium-MRI or $^{23}$Na-MRI), is associated with many challenges due to the composition of tissue and the nuclear properties of the molecule. This section will describe background information regarding the difficulties of sodium-MR imaging and particular procedures that have been employed to facilitate quantification and detection of sodium.

## 1.5.1      Difficulties of Sodium-MRI

Sodium-MR imaging is a technique used to quantify the concentration of sodium in tissues. One of the basic properties required for MR imaging is the property of a non-zero spin-value (magnetic dipole moment) for a nucleus. Sodium possesses a nuclear spin of $\frac{3}{2}$ and 100% of the nuclei exist naturally in this state (as $^{23}$Na). However, certain hurdles make sodium-MRI challenging. These include the low tissue concentration of $^{23}$Na ions in the body, its low gyromagnetic ratio (11.262 MHz T$^{-1}$) and the $\frac{3}{2}$ nuclear spin. Depending on assumptions related to noise during detection, SNR in MRI is approximately proportional to GMR$^{5/2}$. The average intracellular sodium concentration in humans is

approximately 10-15 mmol/L, while the extracellular concentration is approximately 140 mmol/L. A weighted average, based on the volumes of each cellular space, results in a whole-body healthy tissue sodium concentration (TSC) of $\sim$ 90 mmol/L. In contrast, the concentration of water-associated protons is approximately 80 mol/L in tissues, which is a factor of $10^3$ higher than that of sodium nuclei.

Sodium nuclei possess an intrinsic spin of $\frac{3}{2}$ and therefore exhibit an electric quadrupolar moment in addition to a magnetic dipole moment. This additional nuclear moment leads to bi-exponential $T_2$ relaxation of sodium. Bi-exponential decay describes a magnetization decay with two distinct components: a short ($T_{2,\ fast}$) and long ($T_{2,\ slow}$) component [61]. $T_{2,\ fast}$ is $\sim$ 0.5-5 milliseconds (ms), while $T_{2,\ slow}$ is $\sim$ 15-30 ms. Acquisition of signal from both $T_{2,\ slow}$ and $T_{2,\ fast}$ decay components is necessary for preserving maximum SNR and beneficial for quantifying TSC. To facilitate this, the MRI pulse sequence is optimized for short TEs [62]. When sodium nuclei are exposed to an external magnetic field, the $\frac{3}{2}$ spin of sodium leads to four distinct energy levels (Zeeman energies). These energy levels are: $\frac{3}{2}, \frac{1}{2}, -\frac{1}{2}, -\frac{3}{2}$ and transitions between these levels alters the observed relative amplitudes of $T_{2,\ fast}$ and $T_{2,\ slow}$ relaxation.

## 1.5.2    Quantifying Sodium Concentration with Sodium-MRI

To facilitate *in vivo* sodium imaging of tissue in the body, custom imaging hardware is needed to perform RF excitation and detection of sodium nuclei at their specific Larmor frequency [63]. This hardware must be highly optimized and can be paired with very short echo times in pulse sequences (mentioned in previous section) to maximize possible SNR.

In addition, the sodium RF hardware should not significantly interfere with proton imaging used to acquire morphological images for image registration of regional TSC, mpMRI and histopathology data determined after prostatectomy.

When imaging with sodium-MRI, we require the use of phantoms to quantify the sodium signal. First, assessment of the sensitivity profile of the RF coils is necessary. This is typically done using a large saline bath with a sodium concentration between 100-150 mmol/L. Following this, a procedure described by Axel *et al.* (1987) allows for normalization of the sodium signal based on the location of the voxel relative to the receive coil [64]. In the housing of the receive RF coil itself, reference phantoms are incorporated with known concentrations ranging from 20-150 mmol/L for quantification of absolute tissue sodium concentrations in the voxel of interest.

## 1.6 Objectives, Hypothesis and Goals

The objective of this thesis was to investigate the relationship between *in vivo* tissue sodium concentration and prostate cancer tumour aggression. Tissue sodium concentration was assessed in men with biopsy-proven prostate cancer using sodium-MR. After prostatectomy, whole-mount histopathology sections of the prostate were examined by an expert and lesions were identified by contours and assigned a Gleason grade for aggressiveness. Co-registration of MRI imaging data (TSC, $T_2$-weighted contrast and ADC values) with the histopathology allowed for accurate comparison of lesions to imaging data.

We hypothesized that the endogenous tissue sodium concentration measured in prostate cancer patients would have a significant relationship with histological Gleason score. Specifically, we hypothesized that TSC values would have monotonic, increasing trend with Gleason grade, leading to accurate staging of lesions into low- and high-risk categories based on the acquired TSC data.

The goal of this work was to identify the utility of using TSC as a component of a *non-invasive imaging* assay. In this, sodium-MRI would be employed with mpMRI to aid in prostate cancer lesion detection and subsequent characterization of that lesion's grade *in vivo*. This would give men with low-grade prostate cancer more confidence to choose active surveillance instead of treatment, reducing the frequency of overtreatment in our healthcare system.

# References for Chapter 1

1.      McNeal, J.E., *The zonal anatomy of the prostate.* Prostate, 1981. **2**(1): p. 35-49.

2.      Kai H. Hammerich, G.E.A., Thomas M. Wheeler, *Anatomy of the prostate gland and surgical pathology of prostate cancer*, in *Cambridge University Press*. 2009: Cambridge University. p. 9.

3.      McNeal, J.E., et al., *Zonal distribution of prostatic adenocarcinoma. Correlation with histologic pattern and direction of spread.* Am J Surg Pathol, 1988. **12**(12): p. 897-906.

4.      Muruve, N.A. *Prostate Anatomy*. 2017 10/13/17.

5.      Uhlen, M., et al., *Tissue-based map of the human proteome.* Science, 2015. **347**(6220).

6.      Balk, S.P., Y.J. Ko, and G.J. Bubley, *Biology of prostate-specific antigen.* J Clin Oncol, 2003. **21**(2): p. 383-91.

7.      Stephan, C., B. Ralla, and K. Jung, *Prostate-specific antigen and other serum and urine markers in prostate cancer.* Biochim Biophys Acta, 2014. **1846**(1): p. 99-112.

8.      Ellsworth, P.I. *PSA Test (Prostate Specific Antigen)*. 2018 2/2/2018 [cited 2018 4/4].

9.      Statistics, C.C., *Statistics CCSAC on Cancer Statistics.* 2017.

10.     Sakr, W.A., et al., *Age and racial distribution of prostatic intraepithelial neoplasia.* Eur Urol, 1996. **30**(2): p. 138-44.

11.     Cao, Y. and J. Ma, *Body mass index, prostate cancer-specific mortality, and biochemical recurrence: a systematic review and meta-analysis.* Cancer Prev Res (Phila), 2011. **4**(4): p. 486-501.

12.     Bensimon, L., et al., *Type 2 diabetes and the risk of mortality among patients with prostate cancer.* Cancer Causes Control, 2014. **25**(3): p. 329-38.

13.     Network, N.C.C., *NCCN Guidelines for Patients*. 2016.

14.     Kolata, G., *More Men With Early Prostate Cancer Are Choosing to Avoid Treatment*, in *The New York Times*. 2016: The Science Times.

15.     Gleason, D.F., *Histologic grading of prostate cancer: a perspective.* Hum Pathol, 1992. **23**(3): p. 273-9.

16.     Epstein, J.I., et al., *The 2005 International Society of Urological Pathology (ISUP) Consensus Conference on Gleason Grading of Prostatic Carcinoma.* Am J Surg Pathol, 2005. **29**(9): p. 1228-42.

17.     Epstein, J.I., *Gleason score 2-4 adenocarcinoma of the prostate on needle biopsy: a diagnosis that should not be made.* Am J Surg Pathol, 2000. **24**(4): p. 477-8.

18.     Steinberg, D.M., et al., *Correlation of prostate needle biopsy and radical prostatectomy Gleason grade in academic and community settings.* Am J Surg Pathol, 1997. **21**(5): p. 566-76.

19.     Albertsen, P.C., et al., *Competing risk analysis of men aged 55 to 74 years at diagnosis managed conservatively for clinically localized prostate cancer.* JAMA, 1998. **280**(11): p. 975-80.

20.     Allsbrook, W.C., Jr., et al., *Interobserver reproducibility of Gleason grading of prostatic carcinoma: urologic pathologists.* Hum Pathol, 2001. **32**(1): p. 74-80.

21.     Gordetsky, J. and J. Epstein, *Grading of prostatic adenocarcinoma: current state and prognostic implications.* Diagn Pathol, 2016. **11**: p. 25.

22.     Epstein, J.I., *An update of the Gleason grading system.* J Urol, 2010. **183**(2): p. 433-40.

23.     Kweldam, C.F., et al., *Cribriform growth is highly predictive for postoperative metastasis and disease-specific death in Gleason score 7 prostate cancer.* Mod Pathol, 2015. **28**(3): p. 457-64.

24.     Fajardo, D.A., et al., *Identification of Gleason pattern 5 on prostatic needle core biopsy: frequency of underdiagnosis and relation to morphology.* Am J Surg Pathol, 2011. **35**(11): p. 1706-11.

25.     National Comprehensive Cancer, N., *Prostate cancer. NCCN clinical practice guidelines in oncology.* J Natl Compr Canc Netw, 2004. **2**(3): p. 224-48.

26.     Bechis, S.K., et al., *Personalized medicine for the management of benign prostatic hyperplasia.* J Urol, 2014. **192**(1): p. 16-23.

27.     Bostwick, D.G. and I. Meiers, *Atypical small acinar proliferation in the prostate: clinical significance in 2006.* Arch Pathol Lab Med, 2006. **130**(7): p. 952-7.

28.     Ruska, K.M., J. Sauvageot, and J.I. Epstein, *Histology and cellular kinetics of prostatic atrophy.* Am J Surg Pathol, 1998. **22**(9): p. 1073-7.

29.     Kash, D.P., et al., *Utility of digital rectal examination, serum prostate specific antigen, and transrectal ultrasound in the detection of prostate cancer: a developing country perspective.* Asian Pac J Cancer Prev, 2014. **15**(7): p. 3087-91.

30. Catalona, W.J., et al., *Measurement of prostate-specific antigen in serum as a screening test for prostate cancer.* N Engl J Med, 1991. **324**(17): p. 1156-61.

31. Pezaro, C., H.H. Woo, and I.D. Davis, *Prostate cancer: measuring PSA.* Intern Med J, 2014. **44**(5): p. 433-40.

32. Gleason, D.F., *Classification of prostatic carcinomas.* Cancer Chemother Rep, 1966. **50**(3): p. 125-8.

33. Rajinikanth, A., et al., *Trends in Gleason score: concordance between biopsy and prostatectomy over 15 years.* Urology, 2008. **72**(1): p. 177-82.

34. Epstein, J.I., et al., *Upgrading and downgrading of prostate cancer from biopsy to radical prostatectomy: incidence and predictive factors using the modified Gleason grading system and factoring in tertiary grades.* Eur Urol, 2012. **61**(5): p. 1019-24.

35. Singh, H., et al., *Predictors of prostate cancer after initial negative systematic 12 core biopsy.* J Urol, 2004. **171**(5): p. 1850-4.

36. Middleton, R.G., et al., *Prostate Cancer Clinical Guidelines Panel Summary report on the management of clinically localized prostate cancer. The American Urological Association.* J Urol, 1995. **154**(6): p. 2144-8.

37. Thomsen, F.B., et al., *Active surveillance for clinically localized prostate cancer--a systematic review.* J Surg Oncol, 2014. **109**(8): p. 830-5.

38. Parker, C., *Active surveillance: an individualized approach to early prostate cancer.* BJU Int, 2003. **92**(1): p. 2-3.

39. Sanyal, C., et al., *Management of localized and advanced prostate cancer in Canada: A lifetime cost and quality-adjusted life-year analysis.* Cancer, 2016. **122**(7): p. 1085-96.

40. Klotz, L., *Prostate cancer overdiagnosis and overtreatment.* Curr Opin Endocrinol Diabetes Obes, 2013. **20**(3): p. 204-9.

41. Yao, S.L. and G. Lu-Yao, *Understanding and appreciating overdiagnosis in the PSA era.* J Natl Cancer Inst, 2002. **94**(13): p. 958-60.

42. Vander Heiden, M.G., L.C. Cantley, and C.B. Thompson, *Understanding the Warburg effect: the metabolic requirements of cell proliferation.* Science, 2009. **324**(5930): p. 1029-33.

43. Warburg, O., F. Wind, and E. Negelein, *The Metabolism of Tumors in the Body.* J Gen Physiol, 1927. **8**(6): p. 519-30.

44. Warburg, O., *On the origin of cancer cells.* Science, 1956. **123**(3191): p. 309-14.

45.      Moreno-Sanchez, R., et al., *Energy metabolism in tumor cells.* FEBS J, 2007. **274**(6): p. 1393-418.

46.      Thulborn, K.R., et al., *Comprehensive MR imaging protocol for stroke management: tissue sodium concentration as a measure of tissue viability in nonhuman primate studies and in clinical studies.* Radiology, 1999. **213**(1): p. 156-66.

47.      Rotin, D., et al., *Requirement of the Na+/H+ exchanger for tumor growth.* Cancer Res, 1989. **49**(1): p. 205-11.

48.      Mager, T., et al., *Transport mechanism and pH regulation of the Na+/H+ antiporter NhaA from Escherichia coli: an electrophysiological study.* J Biol Chem, 2011. **286**(26): p. 23570-81.

49.      Gatenby, R.A., et al., *Acid-mediated tumor invasion: a multidisciplinary study.* Cancer Res, 2006. **66**(10): p. 5216-23.

50.      Reshkin, S.J., et al., *Na+/H+ exchanger-dependent intracellular alkalinization is an early event in malignant transformation and plays an essential role in the development of subsequent transformation-associated phenotypes.* FASEB J, 2000. **14**(14): p. 2185-97.

51.      Ouwerkerk, R., et al., *Tissue sodium concentration in human brain tumors as measured with 23Na MR imaging.* Radiology, 2003. **227**(2): p. 529-37.

52.      Ouwerkerk, R., et al., *Elevated tissue sodium concentration in malignant breast lesions detected with non-invasive 23Na MRI.* Breast Cancer Res Treat, 2007. **106**(2): p. 151-60.

53.      Bartha, R., J.F. Megyesi, and C.J. Watling, *Low-grade glioma: correlation of short echo time 1H-MR spectroscopy with 23Na MR imaging.* AJNR Am J Neuroradiol, 2008. **29**(3): p. 464-70.

54.      Haacke, E.M., et al., *Magnetic Resonance Imaging: Physical Principles and Sequence Design.* 1999: Wiley.

55.      Bernstein, M.A., K.F. King, and Z.J. Zhou, *Handbook of MRI pulse sequences.* 2004, Amsterdam ; Boston: Academic Press. xxii,1017 p.

56.      Fornasa, F., *Diffusion-weighted Magnetic Resonance Imaging: What Makes Water Run Fast or Slow?* J Clin Imaging Sci, 2011. **1**: p. 27.

57.      Weinmann, H.J., et al., *Tissue-specific MR contrast agents.* Eur J Radiol, 2003. **46**(1): p. 33-44.

58.      Hermann, P., et al., *Gadolinium(III) complexes as MRI contrast agents: ligand design and properties of the complexes.* Dalton Trans, 2008(23): p. 3027-47.

59.    de Rooij, M., et al., *Accuracy of multiparametric MRI for prostate cancer detection: a meta-analysis.* AJR Am J Roentgenol, 2014. **202**(2): p. 343-51.

60.    Nagel, A.M., et al., *The potential of relaxation-weighted sodium magnetic resonance imaging as demonstrated on brain tumors.* Invest Radiol, 2011. **46**(9): p. 539-47.

61.    Madelin, G., et al., *Sodium MRI: methods and applications.* Prog Nucl Magn Reson Spectrosc, 2014. **79**: p. 14-47.

62.    Bangerter, N.K., et al., *Sodium MRI radiofrequency coils for body imaging.* Nmr in Biomedicine, 2016. **29**(2): p. 107-118.

63.    Farag, A., et al., *Unshielded asymmetric transmit-only and endorectal receive-only radiofrequency coil for (23) Na MRI of the prostate at 3 tesla.* J Magn Reson Imaging, 2015. **42**(2): p. 436-45.

64.    Axel, L., J. Costantini, and J. Listerud, *Intensity correction in surface-coil MR imaging.* AJR Am J Roentgenol, 1987. **148**(2): p. 418-20.

Chapter 2

# 2 Characterization of Clinical Human Prostate Cancer Lesions Using 3.0-T Sodium-MRI Registered to Gleason-Graded Whole-Mount Histopathology

*Nolan C. Broeke, Justin Peterson, Joseph Lee, Peter Martin, Adam Farag,*

*Jose Gomez-Lemus, Madeleine Moussa, Mena Gaed, Joseph Chin, Stephen*

*Pautler, Aaron Ward, Glenn Bauman, Robert Bartha, Timothy J. Scholl*

## 2.1 Abstract

Overtreatment of prostate cancer is a significant problem in the health care of men. Development of *non-invasive* imaging tools for improved characterization of prostate lesions can reduce overtreatment. We have previously built custom sodium-MRI hardware to image and quantify tissue sodium concentration (TSC) in the human prostate from sodium-MRI. In this study, we have evaluated sodium-MRI and mpMRI data (including diffusion-weighted and $T_2$-weighted imaging) from a patient cohort of ten men with biopsy-proven prostate cancer. All imaging data were co-registered to Gleason-graded post-prostatectomy histology, as the standard for prostate cancer lesion characterization. TSC and $T_2$ data were assessed using percent changes from healthy tissue of the same patient ($\Delta$TSC, $\Delta T_2$). Significant changes in $\Delta$TSC, ADC values and $\Delta T_2$ were observed between Gleason scores in averaged cohort data ($p < 0.05$). Evaluation of the correlation of $\Delta$TSC, ADC, and $\Delta T_2$ data sets with Gleason scoring revealed that only the correlation between $\Delta$TSC and Gleason score was statistically significant ($r_s = 0.791$, $p < 0.01$), whereas the correlations of ADC and $\Delta T_2$ with Gleason score were not ($r_s = -0.306$, $p = 0.079$ and $r_s = -0.069$, $p = 0.699$, respectively). In addition, all individual patients showed

an increasing trend of ΔTSC with Gleason score. The results of this study suggest that TSC assessed by sodium-MRI has utility as a *"non-invasive imaging assay"* to accurately characterize prostate cancer lesions. Sodium-MRI can provide useful complementary information to mpMRI, ultimately leading to increased confidence of men with low-risk disease to opt for active surveillance instead of treatment.

## 2.2  Introduction

One in seven men will develop prostate cancer (PCa) in their lifetime, making it the most common non-cutaneous malignancy in males [1]. However, overdiagnosis of clinically insignificant disease has been a concern since the introduction of the prostate-specific antigen (PSA) screening test [2-4]. Overdiagnosis has been shown to negatively affect patient quality of life and increase the healthcare costs for society [5]. For men with suspected prostate cancer, a standard approach involves a transrectal ultrasound (TRUS)-guided biopsy to extract 12 cores [6] for histological Gleason scoring. The current system for grading PCa is the Gleason Scoring System. The combination of the primary and secondary cancer grades present is inherently related to tumour aggression; making the Gleason score the strongest prognostic and predictive factor for the disease [7-9]. However, biopsy only samples approximately 0.5% of the prostate, which carries a 30-40% risk of under sampling clinically significant lesions [10-12]. Therefore, the use of non-surgical imaging-based methods to accurately discriminate between low- and high-grade lesions would be useful to reduce repeated negative biopsies, to place patients in the proper treatment streams and to surveil low-risk cancer. This, in turn will optimize patient outcomes and the use of health care resources. Currently, multi-parametric magnetic resonance imaging (mpMRI) contrasts such as $T_2$-weighted, diffusion-weighted magnetic resonance imaging (DWI), and dynamic contrast enhanced MRI (DCE-MRI) aid physicians in PCa lesion detection [13-15]. Diffusion-weighted imaging signal intensity is based on measurement of the Brownian motion of water molecules in a voxel [16]. Inverse correlations between apparent diffusion coefficient (ADC) signal intensity and cell count in tumours were shown by Surov *et al.* [17]. The strength of these correlations was seen to

be dependent on the location of the cancer tissue, with only moderate inverse correlations recorded in prostatic cancer [17]. $T_2$-weighted prostate MRI produces anatomical images with high spatial-resolution and it allows for precise differentiation of the different zones of this gland. On $T_2$-weighted images of the prostate, lesions in the peripheral zone typically show a hypo-intense signal compared to healthy tissue [14]. The degree of these differences can vary with Gleason score. However, regions of lower signal do not necessarily represent malignancies. Prostate lesions arising from scars, atrophy, hyperplasia, chronic prostatitis, and post-biopsy hemorrhage have been shown to also exhibit low signal intensity on $T_2$-weighted images [18].

These techniques provide high spatial resolution, but their specificity is often insufficient to localize malignant lesions and confidently assign tumour grades to these foci. Thus, there is a need for new imaging biomarkers to provide complementary information about the location and grade of intraprostatic cancer. Tissue sodium concentration (TSC) has been shown to be a sensitive indicator of cell integrity and energy metabolism [19-21]. The link between increased activity of a sodium-proton ($Na^+/H^+$) antiport [22, 23] and sodium-potassium ($Na^+/K^+$) ATPase [19, 24] and tumour malignancy has been well studied. TSC measured by sodium ($^{23}$Na) MRI can provide regional information about intracellular and extracellular changes within tissue. While TSC has been examined in brain and breast cancer [21, 25, 26], TSC has not yet been compared to tumour grade in human PCa. Our lab has previously developed $^{23}$Na imaging hardware comprised of a transmit-only asymmetrical birdcage coil and a receive-only endorectal coil, providing sufficient sensitivity to image endogenous sodium throughout the human prostate [27]. In this research study, mpMRI and sodium-MRI data were collected from

men with biopsy-proven prostate cancer prior to prostatectomy. These imaging data were subsequently registered to graded PCa lesions identified on whole-mount histopathological sections through a validated registration pipeline [28]. Tissue sodium concentration, ADC values, and $T_2$-weighted signal intensity were compared and correlated with histological tumour grade to assess the utility of TSC for improved characterization of prostate lesions.

## 2.3  Methodology

### 2.3.1   Patients

Ten male patients (aged 63±5) (Table 1) selected through previous biopsy to have PCa of Gleason score 7 or less were recruited between 2013 and 2016 in conjunction with a multi-modality, image-guided prostate cancer study (IGPC-2) [28]. This selection process intentionally targeted a patient population including low to intermediate risk groups, where additional characterization of tumour aggression would be particularly useful for risk stratification decisions where mpMRI provides less reliable guidance. In addition to standard exclusion criteria for MR studies (implanted devices etc.), men were excluded from this study if they had prior therapy for PCa, use of 5-alpa reductase inhibitors within 6 months of the start of the study, a prostate volume greater than 68 cc, allergies to contrast agents and other administered agents, insufficient renal function, and a residual bladder volume greater than 150 mL. Patients were instructed to drink 30 mL of milk of magnesia the night before the MR exam and to fast 12 hours prior to the exam. Sodium-MRI was performed in combination with mpMRI, including the following contrasts: diffusion-weighted, $T_2$-weighted, and post-Gadolinium $T_1$-weighted imaging, however DCE was not included in the data analysis. *Ex vivo* imaging of the prostatectomy specimens included $T_1$- and $T_2$-weighted imaging.

**Table 2-1. Clinical data for the ten patients analyzed in this study.**

| Category | Patient 1 | Patient 2 | Patient 3 | Patient 4 | Patient 5 | Patient 6 | Patient 7 | Patient 8 | Patient 9 | Patient 10 |
|---|---|---|---|---|---|---|---|---|---|---|
| Age | 65 | 64 | 53 | 66 | 64 | 66 | 68 | 59 | 57 | 66 |
| ***Pre-Treatment Procedures*** | | | | | | | | | | |
| Pre-biopsy PSA (ng/mL) | 14.96 | 5.05 | 4.22 | 6.13 | 4.33 | 25.49 | 4.66 | 3.67 | 1.05 | 4.16 |
| Primary Pattern | 3 | 3 | 3 | 3 | 4 | 3 | 3 | 3 | 3 | 3 |
| Secondary Pattern | 4 | 4 | 4 | 4 | 3 | 4 | 4 | 4 | 4 | 4 |
| Overall Gleason Score | 7 | 7 | 7 | 7 | 7 | 8 | 7 | 7 | 7 | 6 |
| Prostate Volume (cc) | 45 | 30 | 25 | 65 | 39 | 57 | 23 | 22.6 | 48.32 | 37 |
| Clinical T-Stage | cT2c | cT2c | cT1c | cT2b | cT1c | cT2a | cT2b | cT1c | cT1c | cT2a |
| ***Screening Bloodwork*** | | | | | | | | | | |
| Creatinine (µmol/L) | 76 | 64 | 92 | 90 | 84 | 69 | 105 | 69 | 77 | 75 |
| eGFR (mL/min/1.73m$^2$) | 95 | 116 | 79 | 78 | 85 | 106 | 65 | 108 | 96 | 96 |
| Urea (mmol/L) | 5.1 | 3.9 | 6.9 | 5.2 | 9.2 | 5 | 9.1 | 6.1 | 6.5 | 6.1 |
| Residual Bladder Volume (mL) | 78 | 224 | 165 | 49 | 20 | 18 | 0 | 32 | 92 | 0 |
| ***Post Radical Prostatectomy*** | | | | | | | | | | |
| Primary Pattern | 3 | 3 | 3 | 3 | 4 | 3 | 3 | 3 | 3 | 3 |
| Secondary Pattern | 4 | 4 | 4 | 4 | 3 | 4 | 4 | 4 | 4 | 4 |
| Tertiary Pattern | 5 | none | none | 5 | none | none | none | none | none | none |
| Overall Gleason Score | 7 | 7 | 7 | 7 | 7 | 7 | 7 | 7 | 7 | 7 |
| Pathological T-Stage | pT3b | pT3a | pT2c | pT3b | pT3a | pT3a | pT2c | pT2c | pT2c | pT2c |
| Pathological N-Stage | pN0 | pN0 | pN0 | pN0 | pN0 | pN0 | pN0 | pN0 | pN0 | pNX |
| Pathological M-Stage | pMx | pMx | pMx | pMx | pMx | pMx | pMx | pMx | pMx | pMx |

## 2.3.2 *In Vivo* multi-parametric MR Imaging

All magnetic resonance imaging data for this study were acquired at a field strength of 3 T (General Electric Healthcare Discovery MR750 3.0 T, Milwaukee, WI, USA). High-resolution $T_2$-weighted images (TE: 162 ms, TR: 2000 ms, Field of view (FOV): 140 × 140 mm, voxel size: 0.44 × 0.73 × 1.4 mm, flip angle: 90˚) were acquired using a 3D Cube sequence, and the standard inflatable ^{1}H endorectal (ER) coil. This image set was used for registration of sodium images to histopathology. Apparent diffusion coefficient (ADC) maps were obtained using a 2D Spin-Echo sequence, the inflatable ^{1}H endorectal coil, and the following parameters: TE: 68.1 ms, TR: 5600 ms, FOV: 140 × 140 mm, voxel size: 1.1 × 0.55 × 3.6 mm, flip angleK 90˚, and *b*-values of 100 and 800 s/mm^{2}.

## 2.3.3 Sodium Imaging

Sodium imaging was performed using a bespoke endorectal receive-only radiofrequency (RF) coil and an asymmetric transmit-only birdcage RF coil [27]. A topical anesthetic, Xylocaine (2%) was applied to the patient prior to insertion of the ER coil. Following insertion of the [23]Na ER coil a set of ^{1}H, axial $T_2$-weighted images were initially acquired using a 2D Fast Spin-Echo sequence (TE: 139.2 ms, TR: 5300 ms, FOV: 140 × 140 mm, voxel size: 1.09 × 1.09 × 3 mm, and flip angle: 90˚) to provide morphological context for the sodium images. This enabled accurate registration of the sodium images to the high-resolution $T_2$-weighted image set. [1]H imaging with the [23]Na hardware was possible because of the unshielded design of the transmit-only RF coil, along with proper detuning of the receive-only ER coil. Sodium images were then acquired using a broad-banded 3D

Fast Gradient-Recalled-Echo sequence with the following parameters: TE: 1.5 ms, TR: 80 ms, FOV: 140 × 140 mm, voxel size: 4.4 × 4.4 × 6 mm, and flip angle: 85˚. Three calibration vials containing 30, 90, and 150 mmol/L of sodium chloride (NaCl) solutions were incorporated into the rigid $^{23}$Na ER coil. These solutions were used to scale the sodium signal from the prostate tissues to absolute concentrations per Farag *et al*. [27]. Sodium images were normalized to the sensitivity profile of the $^{23}$Na ER surface coil, acquired in a separate measurement in a procedure described by Axel *et al.* [29].

## 2.3.4   *Ex Vivo* Imaging

Following radical prostatectomy, prostate specimens were encased in a syringe of Christo-Lube MCG 1046, an MR-invisible fluorinated lubricant, to minimize magnetic susceptibility artifacts at the tissue-prostate boundary. The specimens were then imaged on the same 3 Tesla scanner used for *in vivo* imaging. Both $T_1$-weighted (TE: 2.34 ms, TR: 6.41, FOV: 140 × 140 mm, voxel size: 0.73 × 0.55 × 0.6 mm, flip angle: 15˚) and $T_2$-weighted (TE: 114 ms, TR: 2000 ms, FOV: 140 × 140 mm, voxel size: 0.73 × 0.44 × 0.6 mm, and flip angle: 90˚) images were obtained using a 3D Spoiled Gradient-Recalled-Echo and a 3D Cube sequence, respectively.

## 2.3.5   Whole-Mount Pathology

Dyed cotton threads, treated with paramagnetic contrast agent were used as MRI-visible fiducial prostate markers, which are also visible under microscopic examination. Excised prostate specimens were pierced with three cotton threads through the prostate and seven threads on the surface as fiducial markers. The prostate midglands were then sliced

into ~4-mm transverse sections before paraffin embedding, leaving enough of the apex and base to be sliced in the sagittal plane for routine pathology analysis. Using a microtome, a 4-µm slice was obtained from each section and stained with Haematoxylin and Eosin (H&E). The slides were then scanned at high resolution (0.5-µm isotropic resolution, 24-bit colour) using a bright-field slide scanner (ScanScope GL; Aperio Technologies, Vista, CA, USA) and subsequently contoured for Gleason score by a pathology assistant supervised by a genitourinary pathologist [28, 30].
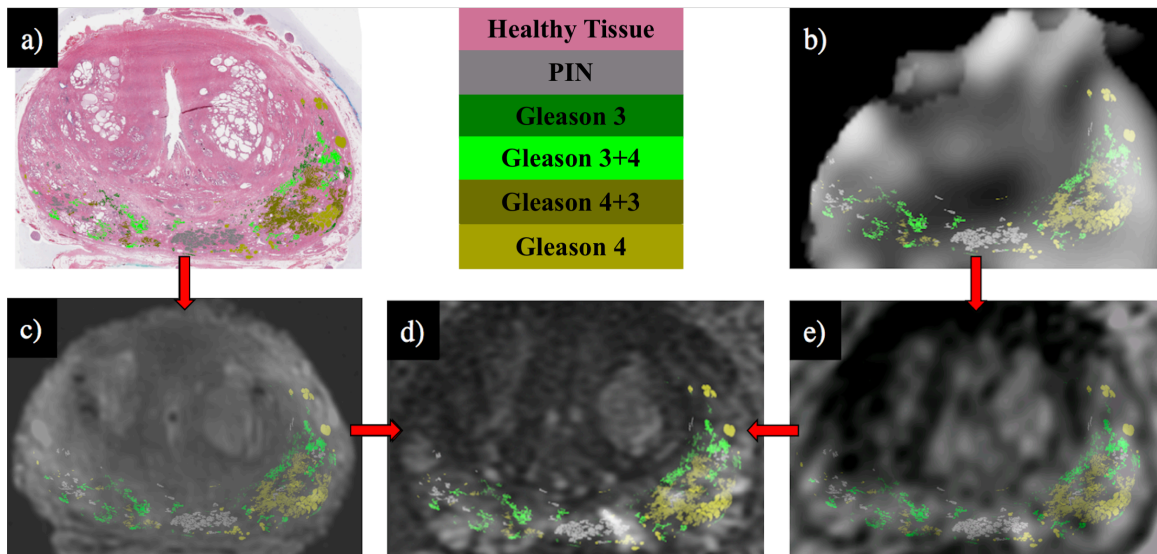


**Figure 2-1. Registration pipeline for all imaging data with Gleason contours overlaid. Whole-mount histopathology (a) and the sodium-MR image (b) are registered to the $T_2$-weighted *ex vivo* (c) and the lower resolution $T_2$-weighted *in vivo* images (e) respectively. The *ex* and *in vivo* images are individually registered to the high resolution $T_2$-weighted *in vivo* image (d). Gleason contour legends are shown in the upper middle panel.**

## 2.3.6    Registration

Co-registration of image data was necessary due to the deformation of the tissue, caused by differing geometries (rigid *vs.* inflatable) of the ER probes and the uncompressed nature of the *ex vivo* tissue. Comparison of the contoured histology to sodium-MRI data, ADC maps and $T_2$-weighted contrast was achieved through a previously reported registration pipeline [28]. Figure 1 outlines all the image contrasts involved and their position along the registration pipeline. ADC is not included in the pipeline figure as it is inherently registered to the high resolution $T_2$-weighted images. All manual registration was performed using 3D Slicer (version 4.3.1) with a non-rigid, interactive thin-plate spline (TPS) extension [31]. Registration involved positioning of approximately 40 fiducial points on physiologically relevant ROI's, such as benign prostatic hyperplasia and cystic spaces, in the two image volumes being co-registered [28]. After fiducial points were finalized, an input and reference volume were chosen, and the input volume was deformed to fit the reference volume according to the fiducial points chosen. The measured error for 3D histopathology reconstruction is 0.7 mm, with an overall *ex vivo* MRI-histopathology co-registration error of ~ 1.5 mm [28], resulting in a total *ix vivo* MRI-histopathology co-registration error of ~ 3 mm.

## 2.3.7    Statistical Analysis

The histology contour masks outlined on each slice for each Gleason grade were overlaid onto co-registered TSC data, ADC maps and $T_2$ images to determine how the data obtained from each image set compares to identified regions of Gleason score. Distinct identified regions are classified in two ways: regions of Gleason pattern completely

encapsulated by either healthy tissue or another Gleason score. Areas of patchy Gleason patterning were segmented into 4-mm$^2$ areas that contained only one Gleason score. TSC, ADC and $T_2$-measurements were collected from four Gleason grades, prostatic intraepithelial neoplasia (PIN), and healthy peripheral zone (PZ) tissue. Healthy peripheral zone tissue is designated as the remaining area of the peripheral zone on the histology slides that has not been identified as cancerous by Gleason grading. The areas (mm$^2$) of Gleason contour coverage on whole-mount histology sections are displayed in Table 2. ADC data are presented as absolute ADC values, while TSC and $T_2$ data are presented as percent changes in TSC ($\Delta$TSC) and $T_2$-contrast ($\Delta T_2$). These values are calculated using equations 2.1 and 2.2, respectively.

$$\Delta\text{TSC} = 100\% \times \frac{(TSC_{Lesion} - TSC_{Healthy})}{TSC_{Healthy}} \qquad \text{Equation 2.1}$$

$$\Delta T_2 = 100\% \times \frac{\left(T_{2_{Lesion}} - T_{2_{Healthy}}\right)}{T_{2_{Healthy}}} \qquad \text{Equation 2.2}$$

Using percent change of TSC and $T_2$-signal rather than absolute signal allows for more direct observation of changes due to changes in lesion stage. Resting *in vivo* sodium levels can be different between individual, dependent on metabolic activity and perfusion. The can result in inter-patient differences in baseline tissue sodium concentrations. Our measurements assess how TSC and $T_2$-contrast change from an individual's baseline levels with increasing Gleason score. All data were imported into GraphPad Prism (GraphPad Software, La Jolla, CA, USA) to test for significant differences in $\Delta$TSC, ADC and $\Delta T_2$ values in relation to Gleason score for both individual patients and averaged data.

Differences were tested using either a one-way analysis of variance (ANOVA) and a follow-up Tukey test or an unpaired $t$-test, depending on the number of Gleason grades present in each individual. For these statistical tests, the $n$ used was equal to the number of identified voxels. SPSS statistical software version 20.0.0 (IBM Co., Armonk, NY, USA) was then used to perform a Spearman's non-parametric ranked correlation; testing the strength of the association between $\Delta$TSC, ADC and $\Delta T_2$ values and Gleason score. For this test, the $n$-value represents the number of patients that had each Gleason score. A Pearson's parametric non-ranked correlation was performed between $\Delta$TSC, ADC and $\Delta T_2$ data to assess the associations between these values. Error bars on individual patient graphs are standard error of the mean. Error bars on patient cohort graphs represent one standard deviation.

## 2.4  Results

We analyzed data from ten patients, all with biopsy proven PCa. Clinically relevant patient data is given in Table 2-1. In the prostatectomy specimens acquired from the 10 cases, 564 distinct identified regions of Gleason graded cancer were found in the peripheral zone based on manual segmentations. The distribution of these identified regions on a per patient basis is shown in Figure 2-2.
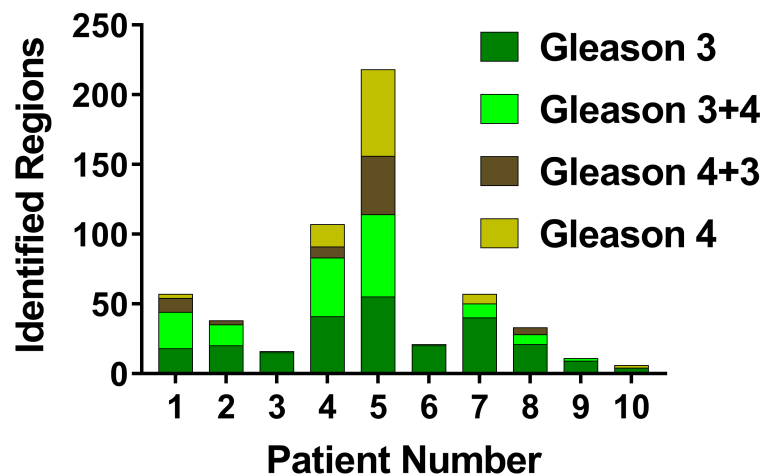


**Figure 2-2. The number and distribution of identified regions of prostate cancer is shown in each of the 10 patients. The identified regions were manually segmented on accurately co-registered whole-mount histopathology using a method described in the statistical analysis section.**

The area of individual lesions measured for analysis ranged from 2.5 $mm^2$ to 122 $mm^2$ on histological sections. All measurement data are displayed in Table 2-2. Across the ten prostates analyzed, nine contained regions of PIN, ten showed Gleason 3, six contained Gleason 3+4, four had Gleason 4+3 patterning, and six showed Gleason 4. Six patients had

clinically significant lesions (> Gleason 7). One patient possessed a high pre-biopsy PSA level and only one Gleason grade of cancer (Patient 6) and therefore was excluded from individual statistical analysis but was included in calculation of the averaged data. Individual patient data from each imaging contrast was collected and displayed in Table 2-2 and graphed in the supplementary information.

**Table 2-2. Percent changes in TSC (ΔTSC), ADC values and percent changes in $T_2$-signal (ΔT₂) are shown for all 10 patients.**

**Data are displayed as ΔTSC, ADC or $\Delta T_2$ ± standard deviation. The size of the Gleason contour from which the imaging data was extracted is shown on the left side of each column (mm²). Weighted averages for all patient data are shown at the bottom of the table with standard deviation**

### TSC Percent Change, ADC values, $T_2$ Percent Change for all Patients

| Case | PIN Histology Area (mm²) | PIN ΔTSC (%) | PIN ADC (×10⁻⁶ mm²/s) | PIN ΔT₂ (%) | Gleason 3 Histology Area (mm²) | Gleason 3 ΔTSC (%) | Gleason 3 ADC (×10⁻⁶ mm²/s) | Gleason 3 ΔT₂ (%) | Gleason 3+4 Histology Area (mm²) | Gleason 3+4 ΔTSC (%) | Gleason 3+4 ADC (×10⁻⁶ mm²/s) | Gleason 3+4 ΔT₂ (%) | Gleason 4+3 Histology Area (mm²) | Gleason 4+3 ΔTSC (%) | Gleason 4+3 ADC (×10⁻⁶ mm²/s) | Gleason 4+3 ΔT₂ (%) | Gleason 4 Histology Area (mm²) | Gleason 4 ΔTSC (%) | Gleason 4 ADC (×10⁻⁶ mm²/s) | Gleason 4 ΔT₂ (%) |
|---|---|---|---|---|---|---|---|---|---|---|---|---|---|---|---|---|---|---|---|---|
| Patient 1 | 88 | 12.5 ± 16 | 1271 ± 182 | -22 ± 30 | 199 | -3.4 ± 17 | 1175 ± 84 | 18 ± 29 | 608 | 5.9 ± 14 | 1178 ± 86 | -12 ± 29 | 1173 | 14.1 ± 20 | 1041 ± 45 | -17 ± 31 | 3 | 37.6 ± 15 | 1372 ± 105 | -21 ± 29 |
| Patient 2 | 881 | -12.5 ± 38 | 1435 ± 137 | -7 ± 46 | 133 | -11.3 ± 28 | 1944 ± 49 | -12 ± 45 | 573 | 7.6 ± 37 | 1554 ± 53 | -11 ± 46 | 72 | 32.8 ± 32 | 1256 ± 52 | 16 ± 46 | | | | |
| Patient 3 | 340 | -6.3 ± 45 | 1159 ± 88 | -17 ± 11 | 39 | 16.9 ± 38 | 1801 ± 100 | -24 ± 12 | 21 | 38.8 ± 39 | 1746 ± 19 | 39 ± 12 | | | | | | | | |
| Patient 4 | 95 | 4.4 ± 22 | 1231 ± 137 | -33 ± 6 | 21 | 13.3 ± 20 | 1281 ± 61 | -16 ± 5 | 173 | 3.9 ± 22 | 1027 ± 29 | -37 ± 6 | 9 | 23.7 ± 19 | 675 ± 25 | -38 ± 6 | | | | |
| Patient 5 | 321 | -1.4 ± 56 | 1335 ± 110 | 20 ± 88 | 101 | 13.7 ± 45 | 1408 ± 102 | 17 ± 84 | 175 | 17.2 ± 48 | 1254 ± 145 | 15 ± 85 | 386 | 33.5 ± 58 | 1424 ± 38 | 9 ± 87 | 250 | 44.5 ± 58 | 1504 ± 85 | 12 ± 87 |
| Patient 6 | | | | | 8 | 16.7 ± 22 | 1750 ± 100 | -16 ± 7 | | | | | | | | | | | | |
| Patient 7 | 10 | -33 ± 98 | 1669 ± 175 | 3 ± 12 | 13 | 16.3 ± 93 | 1742 ± 50 | 4 ± 5 | | | | | | | | | 3 | 30.2 ± 92 | 1229 ± 67 | -8 ± 6 |
| Patient 8 | 27 | -2.8 ± 89 | 1421 ± 107 | -16 ± 10 | 15 | 5 ± 88 | 1352 ± 78 | -25 ± 10 | | | | | | | | | | | | |
| Patient 9 | 620 | 10 ± 458 | 1358 ± 96 | -4 ± 4 | 39 | 13.3 ± 252 | 1268 ± 128 | -3 ± 3 | 15 | 19 ± 249 | 1200 ± 128 | -21 ± 3 | | | | | | | | |
| Patient 10 | 129 | -7.4 ± 42 | 1159 ± 88 | -35 ± 7 | 3 | 8.2 ± 28 | 1124 ± 281 | -4 ± 8 | | | | | 3 | 18 ± 28 | 787 ± 49 | -74 ± 8 | | | | |
| **Average** | **2512** | **-2.9 ± 34** | **1327 ± 24** | **-9 ± 34** | **571** | **1.9 ± 18** | **1469 ± 40** | **-2 ± 16** | **1565** | **8.1 ± 31** | **1350 ± 17** | **-8 ± 31** | **1640** | **19.5 ± 43** | **1159 ± 11** | **-8 ± 43** | **267** | **44.4 ± 22** | **1352 ± 27** | **-23 ± 22** |

Averaging all patient data showed a statistically significant increasing trend in $\Delta$TSC with respect to Gleason score. Furthermore, statistically significant increases in $\Delta$TSC within graded lesions were observable in the data from six of the nine patients ($p < 0.05$). Data from a representative patient (Patient 5) is shown in Figure 2-3, where significant differences were measured between all grades except between Gleason 3 and 3+4 ($p < 0.01$).
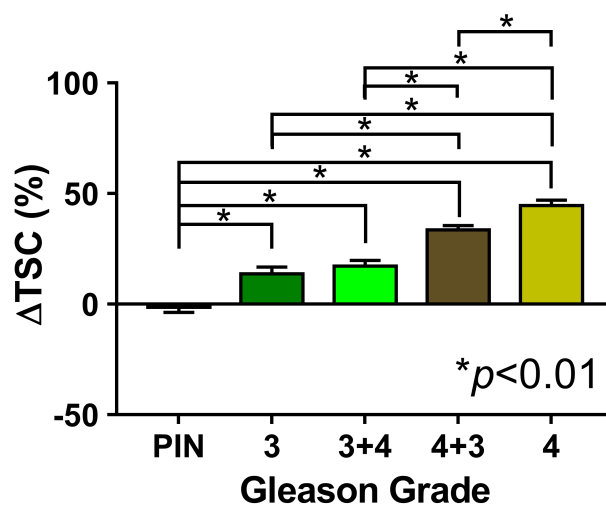


**Figure 2-3. $\Delta$TSC in relation to Gleason grade for a representative case (Patient 5) from our 10-patient cohort. Error bars represent standard error of the mean.**

Intermediate-risk disease (Gleason 7) is frequently classified into treatment schemes based on the predominant identified Gleason pattern. Many clinicians will recommend patients with cancer < Gleason grade 6 (3+3) for active surveillance (AS). Subsequently, men with Gleason scores of 7 and above are candidates for treatment [9, 32]. We report that $\Delta$TSC increased significantly between Gleason 3 and 3+4 in five of the six patients who possessed lesions greater than Gleason 3+4. Graphs of $\Delta$TSC and Gleason

grade from all ten patients are provided in Supplemental Figure 1. ΔTSC patient cohort data were collected and plotted together in Figure 2-4a. These data were correlated with Gleason score using a Spearman's correlation. An $r_s$ value of 0.791 was found showing a significant positive correlation ($p < 0.01$) (Figure 2-7). Weighted averages of ΔTSC were calculated for each Gleason score (Figure 2-4b). These data showed a monotonic increase in ΔTSC with Gleason score. Statistical analysis showed that all differences in average ΔTSC values between Gleason grades were significant ($p < 0.001$). It was observed that the differences in ΔTSC between adjacent Gleason grades becomes larger as identified cancer increases in stage in averaged data.
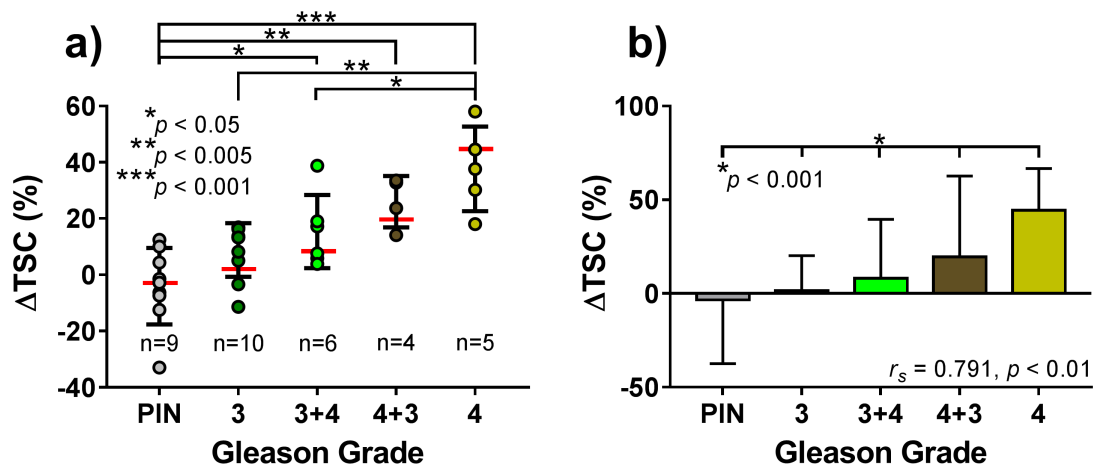


**Figure 2-4. ΔTSC in relation to Gleason score. A) Patient cohort data. Horizontal red line indicates weighted average of all data points. Error bars represent standard deviation. Value of *n* represents the number of patients that possessed a particular Gleason score out of the cohort of 10. b) Weighted average of ΔTSC data, error bars represent one standard deviation. The $r_s$ values shown represents the Spearman's correlation coefficient.**

ADC values were also compared to Gleason score. Individual patient data possessed significant differences between Gleason grades in seven of nine datasets (Supplemental Figure 2). However, a non-monotonic trend between ADC and Gleason score was observed in both individual patients and cohort data (Figure 2-5a). A Spearman's correlation test was performed on patient cohort data, identifying a non-significant correlation of ADC with Gleason score ($r_s$ = -0.306, $p$ = 0.079) (Figure 2-7). Weighted averages of ADC data were calculated from each Gleason score (Figure 2-5b). Non-monotonic, significant differences in ADC values were observed between all the Gleason grades ($p < 0.05$).
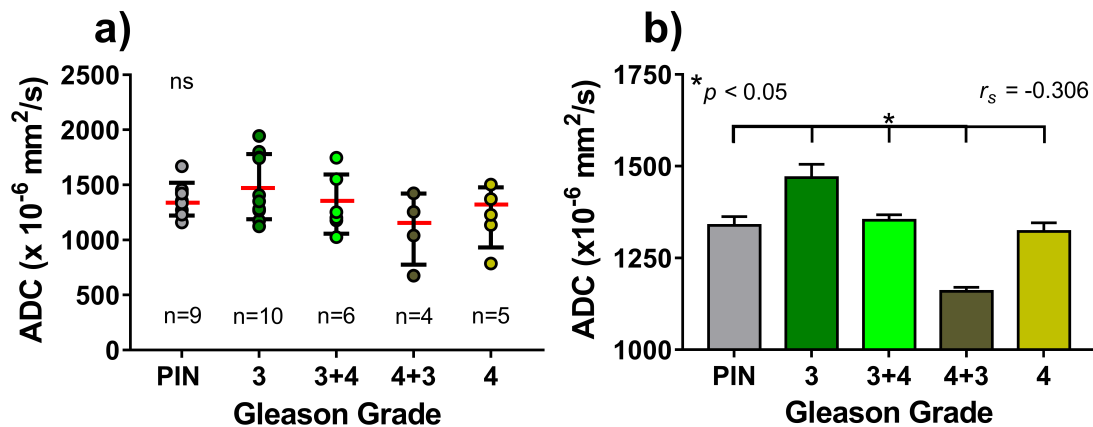


**Figure 2-5. ADC measurements in relation to Gleason score. a) Patient cohort data. Horizontal red line indicates weighted average of all data points. Error bars represent standard deviation. Value of *n* represents the number of patients that possessed a particular Gleason score out of the cohort of 10. b) Weighted average of ADC data, error bars represent one standard deviation. The *r*$_s$ value shown represents the Spearman's correlation coefficient. ns denotes no significance.**

$\Delta T_2$-data were compared to Gleason score using the same percent change method used with TSC data. Individual patient data possessed significant differences between Gleason grades in seven of the nine datasets (Supplemental Figure 3). A Spearman's correlation was performed on patient cohort data (Figure 2-6a), showing a non-significant correlation between $\Delta T_2$ and Gleason grade ($r_s = -0.069$, $p = 0.699$) (Figure 2-7). Weighted averages of $\Delta T_2$-data exhibited non-monotonic, significant differences between Gleason scores (Figure 2-6b).
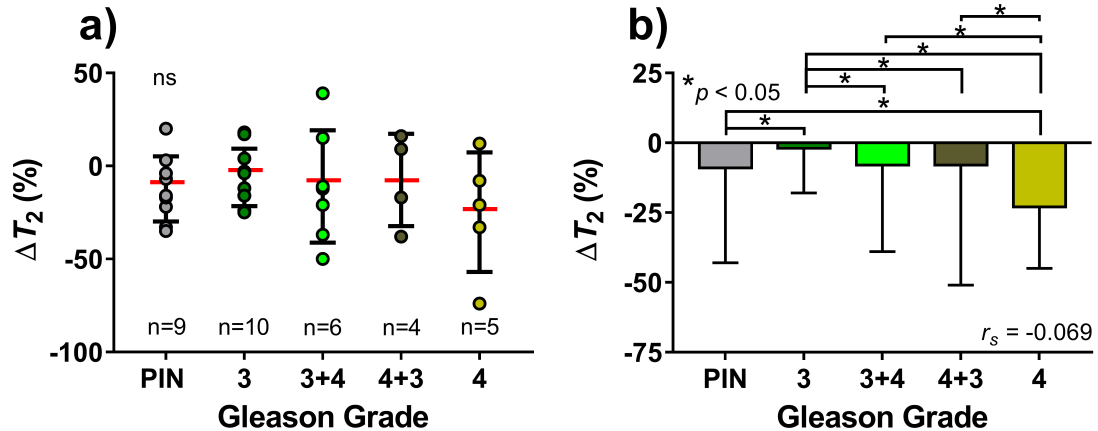


**Figure 2-6. $\Delta T_2$ in relation to Gleason score. a) Patient cohort data. Horizontal red line indicates weighted average of all data points. Error bars represent standard deviation. Value of *n* represents the number of patients that possessed a particular Gleason score out of the cohort of 10. b) Weighted average of $\Delta T_2$ data, error bars represent one standard deviation. The $r_s$ value shown represents the Spearman's correlation coefficient. ns denotes no significance.**
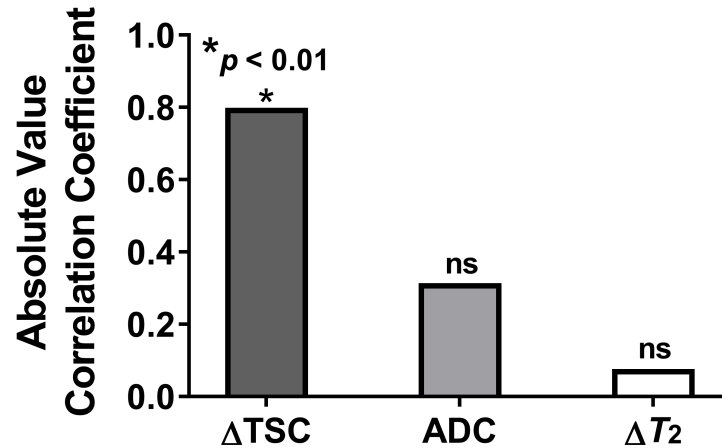
**Figure 2-7. Absolute values of Spearman's non-parametric ranked correlation coefficients for ΔTSC, ADC, and ΔT₂ data. Correlations were performed between imaging data and Gleason grade. No significance denoted by ns.**

We tested the associations between all our imaging data using a Pearson correlation. We observed a statistically significant correlation between ADC and $\Delta T_2$ data ($r = 0.472$, $p = 0.005$). ΔTSC was not correlated with ADC or $\Delta T_2$ ($r = 0.058$, $p = 0.371$, and $r = -0.158$, $p = 0.745$, respectively).

## 2.5  Discussion

We report the first *in vivo* measurement of tissue sodium concentration in human prostate cancer. In addition, this work also represents the first correlation of changes in tissue sodium concentration acquired with sodium-MRI to histologically confirmed Gleason grade using a validated image registration pipeline. Our data show a statistically significant monotonic increase in ΔTSC with increasing Gleason score for individual patients and cohort-averaged patient data. This provides preliminary evidence for the use of sodium-MRI as a *non-invasive* approach to characterize prostate lesions.

Previously, we have demonstrated that TSC can be measured in the human prostate with high signal-to-noise ratio [27]. The gold standard for prostate cancer diagnosis is an invasive 12-core biopsy, sampling a small fraction of the volume of the entire prostate gland. Uncertainty that arises after negative biopsies due to under sampling of potentially aggressive lesions is a major concern for physicians when assigning men to active surveillance. Low-risk, Gleason 6 cancer is the most common diagnosis after biopsy; this grade rarely metastasizes and has a very small associated mortality. This study demonstrates that sodium-MRI of the prostate could provide additional reliable information to *non-invasively* characterize prostate lesions for risk stratification decisions. Patients with lower-risk lesions could be confidently monitored with active surveillance, which might include sodium-MRI, whereas patients in the high-risk category (> Gleason 7) would receive treatment as prescribed by the National Comprehensive Cancer Network's (NCCN) guidelines [33]. Gleason score 7 patients with low-volume grade 4 lesions (Gleason 3+4), who are sometimes excluded from an immediate treatment

recommendation, would benefit from whole-gland lesion characterization by TSC measurement [9]. More reliable *non-invasive* identification of biologically significant foci in the gland may enable clinical decisions including targeted biopsy, focal therapy or focal dose escalation strategies [34-38].

This study involved the development of advanced MRI hardware and a comprehensive data analysis including 3D registration of whole-mount digital histopathology to multiple mpMRI contrasts with a high degree of accuracy (~2 mm). Accurate image registration is imperative to assure that the TSC data measured in a specific ROI are being accurately associated with the Gleason contours on digital histology (see Figure 1). Finally, the development of sensitive integrated TORO RF hardware for sodium imaging was an important development for PCa research [27]. The current study shows that $\Delta$TSC increases with Gleason grade, and this trend was present both in individual data sets and patient cohort data. This increasing trend showed a strong significant correlation with Gleason score ($p < 0.01$), while data from ADC and $\Delta T_2$ did not show strong correlations (Figure 7). While we are unable to associate the $\Delta$TSC correlation with specific cellular changes, it is likely due to cellular reorganization (volume changes) and increased intracellular sodium concentration [21]. With increasing Gleason score, cellular density increases, which leads to a decreased extracellular volume. Cancer cells have been shown to exhibit an increased metabolism, which supplies the cell with enough energy to support accelerated proliferation and enhanced motility [39]. The caveats of this increased metabolism include an upregulation of the sodium-proton ($Na^+/H^+$) antiport [22, 23] and inhibition of a sodium-potassium ($Na^+/K^+$-ATPase) pump [20, 24]. As the tumour cell favors aerobic glycolysis (glycotic energy production over oxidative phosphorylation, even

in the presence of oxygen) [40], this leads to an accumulation of protons within the cell, reducing pH. $Na^+/H^+$ antiport is the major mechanism used to reduce the concentration of intracellular protons [19]. As protons are pumped out, sodium moves into the cell, increasing its intracellular concentration. An acidic extracellular environment is also favored by the cancer cells, as it aids in cell motility [41] and invasiveness [42].

In this study, we performed diffusion weighted imaging (DWI) in conjunction with mpMRI and sodium-MRI. Our DWI data shows that ADC values were not strongly correlated with Gleason score. Data from individual patient, patient cohort data, and cohort average data showed little association between ADC measurements and Gleason score. The ADC measurements recorded in this study agreed with values previously reported in prostate cancer by Hambrock *et al.* [13]. Previous studies have shown that ADC can be used as an imaging biomarker of cell density in glioma, ovarian and lung cancer; however, only moderate correlations were seen in prostate cancer between ADC and cell density [17]. Other research has demonstrated limitations in characterizing dispersed prostatic lesions from normal tissue in the peripheral zone using $T_2$-signal change [43]. This study examined changes in $T_2$-weighted contrast in relation to Gleason grade. Changes in $T_2$-weighted contrast in the prostate can be due to many factors. Kirkham *et al.* showed that benign abnormalities like chronic prostatitis, hyperplasia, scars, atrophy and post-biopsy hemorrhage all lead to hypo-intense signal in $T_2$-weighted images. We observed a weak and insignificant correlation coefficient between $\Delta T_2$ data and Gleason score; however, all averaged $\Delta T_2$ data in lesions were negative, indicating that signal did decrease in lesions compared to healthy tissue. This result has been reported in the literature [44]. The decrease in $T_2$-signal was not correlated with Gleason grade. Patient cohort data displayed a

statistically significant correlation between ADC and $\Delta T_2$. Comparisons between ADC and $T_2$-contrast have been reported in the literature with similar results [44]. Additionally, we showed that ADC and $\Delta T_2$ were both not significantly associated with TSC. The correlation between ADC and $\Delta T_2$ is likely a correlation between cellular density measurements. However, cell density information alone doesn't necessarily provide reliable characterization of a lesion [43]. The addition of $\Delta$TSC to supplement mpMRI has the potential for *non-invasive* lesion characterization. Further, $\Delta$TSC has imminent translational potential to help direct image guided biopsy. Sodium-MRI affords clinicians accurate, *non-invasive* lesion classification; this may help with biopsy needle trajectory planning, decreasing under sampling of clinically significant foci and repeated negative biopsies.

In the current study, the spatial resolution of sodium-MRI was ~5 mm$^3$ vs. ~0.5 mm$^3$ for proton imaging. A broad-banded Fast Gradient-Recalled-Echo pulse sequence with a Cartesian *k*-space trajectory was employed in this study. 3D-Spiral or radial pulse sequences, which are optimized for fast $T_2$ relaxation and efficient coverage of *k*-space for sodium-MRI, have demonstrated the potential for improved SNR [45-47]. Further development in this area could potentially increase spatial resolution and/or reduce acquisition times for sodium-MRI in the prostate. An inherent limitation of a surface ER coil is the receive profile, in which the signal requires sensitivity correction due to the inhomogeneous receive profile. This is an issue for all prostate MRI (including ^{1}H MR), where high-resolution imaging often requires the use of an ER coil. Our $\Delta$TSC data was not affected by this problem as we corrected for the sensitivity profile of the rigid sodium ER coil before analysis. The same correction was not performed on $\Delta T_2$ data, which was

acquired with a separate inflatable (non-rigid) $^1$H ER coil. As a result, these data may be subject to small errors. However, all identified regions analyzed in this study were situated within the peripheral zone. The close-proximity of the peripheral zone to the ER coil reduces the possible error in $\Delta T_2$ data without sensitivity correction. Future work can look at previously acquired DCE imaging data, comparing metrics from the gadolinium-enhanced contrast to the accurately co-registered histological Gleason contours.

In conclusions, this research has demonstrated statistically significant increases in *in-vivo* $\Delta$TSC with increasing Gleason grade in individual patients. Accurate assessment of lesions on an individual basis is important if sodium-MRI is to be used to characterize tumour grade clinically. Further, a strong correlation was found between $\Delta$TSC and Gleason score in patient cohort data along with monotonic, statistically significant increases in $\Delta$TSC when cohort data were averaged together. The combination of sodium-MRI with mpMRI to form a *non-invasive imaging assay* promises improved detection, characterization and surveillance of prostate lesions, which will ultimately increase the confidence of men with early-stage disease to choose active surveillance instead of radical treatment.

## 2.6  Acknowledgement

We acknowledge the valuable assistance of Clinical Research Associates, Ashley Foster and Stephanie Horst, with patient recruitment and research assistance, Cathie Crukley, for preparation of the prostates for *ex vivo* imaging and pathology. We would also like to extend our gratitude to Professor Wenqing He for input with the statistical analysis of our data. We would like to thank the members of the Translational Imaging Research Facility at the Robarts Research Institute, including MR Technologists, Dave Reese and Trevor Szekeres for their assistance imaging the patients used in this study. Finally, we would also like to acknowledge the contributions of Dr. Cesare Romagnoli, who was instrumental in fostering this research in its infancy and who has left us much too soon. He is missed by all his collaborators. We dedicate this manuscript to his memory.

We also thank the following sources of funding, which supported this research project: The Ontario Institute for Cancer Research, and a Discovery Grant from The Natural Sciences and Engineering Research Council of Canada (Scholl).

## 2.7 Supplementary Figures



**Figure 2-8. Supplementary figure 1. ΔTSC in relation to Gleason grade for all 10 individual patient data sets. Error bars represent standard error of the mean. No significance is denoted by ns.**
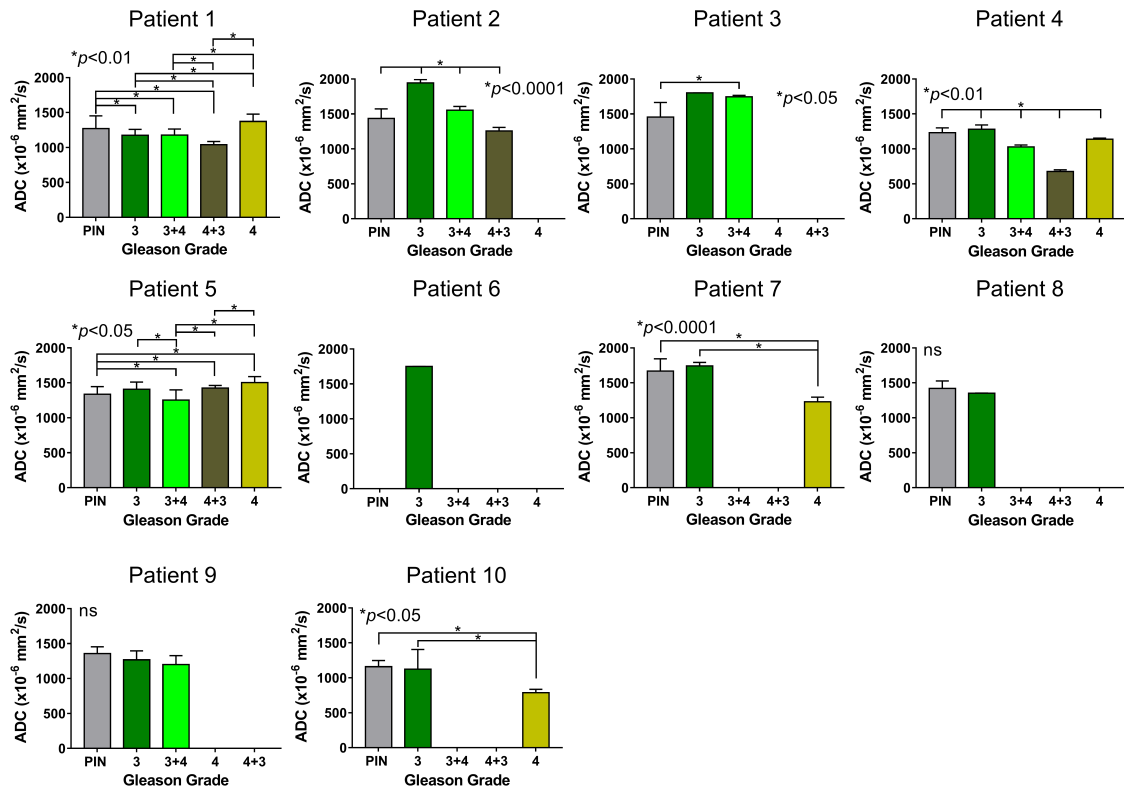
**Figure 2-9. Supplementary figure 2. ADC values in relation to Gleason grade for all 10 individual patient data sets. Error bars represent one standard deviation. No significance is denoted by ns.**
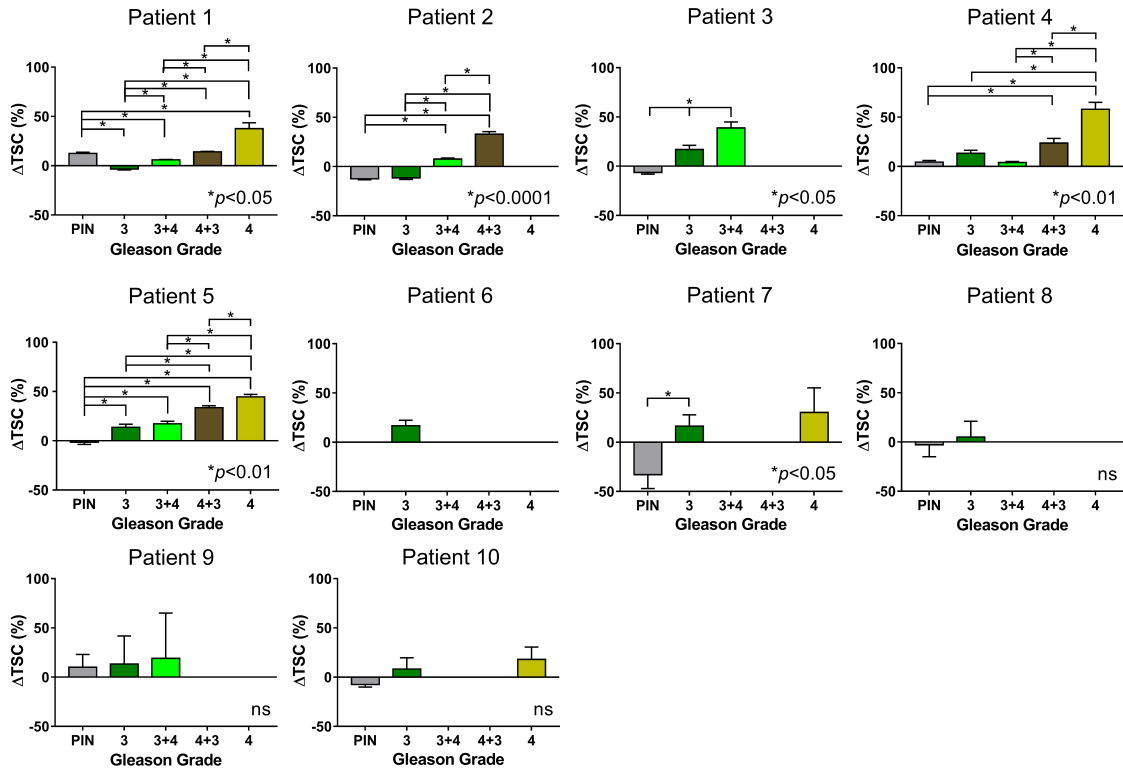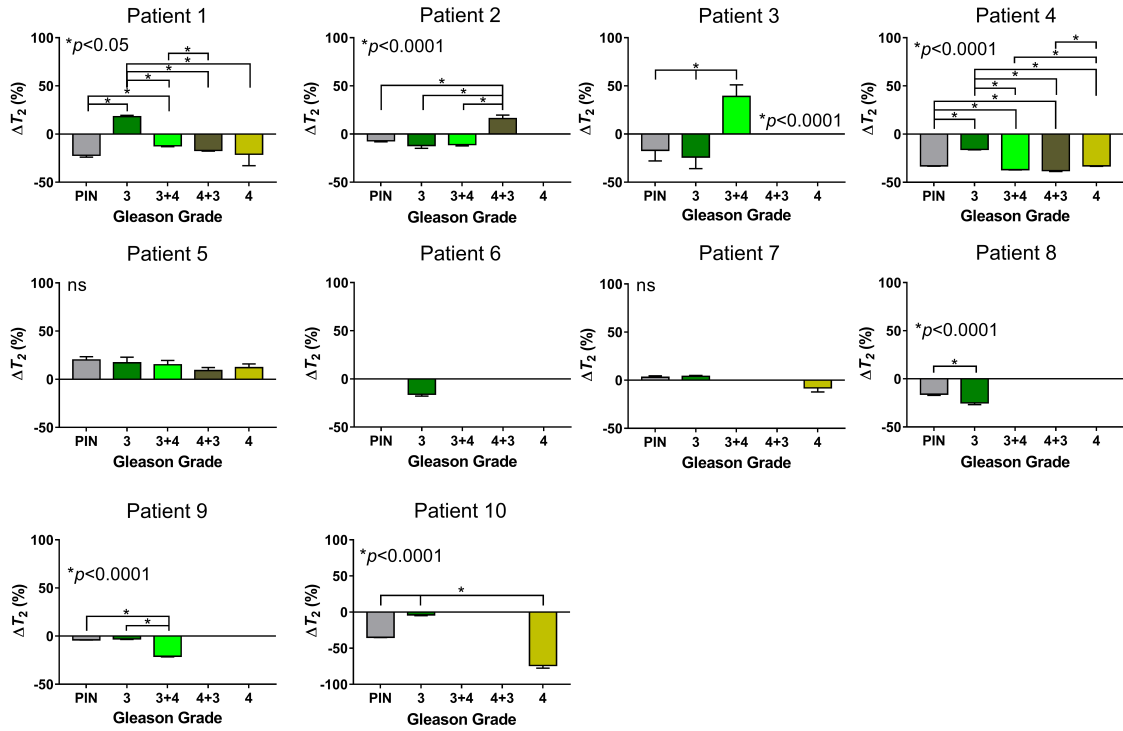
**Figure 2-10. Supplemental Figure 3. $\Delta T_2$ values in relation to Gleason grade for all 10 individual patient data sets. Error bars represent standard error of the mean. No significance is denoted by ns.**

## References for Chapter 2

1.      Statistics, C.C., *Statistics CCSAC on Cancer Statistics.* 2017.

2.      Draisma, G., et al., *Lead time and overdiagnosis in prostate-specific antigen screening: importance of methods and context.* J Natl Cancer Inst, 2009. **101**(6): p. 374-83.

3.      Etzioni, R., et al., *Overdiagnosis due to prostate-specific antigen screening: lessons from U.S. prostate cancer incidence trends.* J Natl Cancer Inst, 2002. **94**(13): p. 981-90.

4.      Heijnsdijk, E.A., et al., *Overdetection, overtreatment and costs in prostate-specific antigen screening for prostate cancer.* Br J Cancer, 2009. **101**(11): p. 1833-8.

5.      Dragomir, A., F.L. Cury, and A.G. Aprikian, *Active surveillance for low-risk prostate cancer compared with immediate treatment: a Canadian cost comparison.* CMAJ Open, 2014. **2**(2): p. E60-8.

6.      Taira, A.V., et al., *Performance of transperineal template-guided mapping biopsy in detecting prostate cancer in the initial and repeat biopsy setting.* Prostate Cancer Prostatic Dis, 2010. **13**(1): p. 71-7.

7.      Bjartell, A., *Words of wisdom. The 2005 International Society of Urological Pathology (ISUP) Consensus Conference on Gleason Grading of Prostatic Carcinoma.* Eur Urol, 2006. **49**(4): p. 758-9.

8.      Gleason, D.F., *Histologic grading of prostate cancer: a perspective.* Hum Pathol, 1992. **23**(3): p. 273-9.

9.      Morash, C., et al., *Active surveillance for the management of localized prostate cancer: Guideline recommendations.* Can Urol Assoc J, 2015. **9**(5-6): p. 171-8.

10.     Scattoni, V., et al., *Extended and saturation prostatic biopsy in the diagnosis and characterisation of prostate cancer: a critical analysis of the literature.* Eur Urol, 2007. **52**(5): p. 1309-22.

11.     Sedelaar, J.P., et al., *Transrectal ultrasound in the diagnosis of prostate cancer: state of the art and perspectives.* Eur Urol, 2001. **40**(3): p. 275-84.

12.     Djavan, B., et al., *Prospective evaluation of prostate cancer detected on biopsies 1, 2, 3 and 4: when should we stop?* J Urol, 2001. **166**(5): p. 1679-83.

13.     Hambrock, T., et al., *Relationship between apparent diffusion coefficients at 3.0-T MR imaging and Gleason grade in peripheral zone prostate cancer.* Radiology, 2011. **259**(2): p. 453-61.

14.    Hoeks, C.M., et al., *Prostate cancer: multiparametric MR imaging for detection, localization, and staging.* Radiology, 2011. **261**(1): p. 46-66.

15.    Weidner, A.M., et al., *Value of multiparametric prostate MRI of the peripheral zone.* Z Med Phys, 2011. **21**(3): p. 198-205.

16.    Fornasa, F., *Diffusion-weighted Magnetic Resonance Imaging: What Makes Water Run Fast or Slow?* J Clin Imaging Sci, 2011. **1**: p. 27.

17.    Surov, A., H.J. Meyer, and A. Wienke, *Correlation between apparent diffusion coefficient (ADC) and cellularity is different in several tumors: a meta-analysis.* Oncotarget, 2017. **8**(35): p. 59492-59499.

18.    Kirkham, A.P., M. Emberton, and C. Allen, *How good is MRI at detecting and characterising cancer within the prostate?* Eur Urol, 2006. **50**(6): p. 1163-74; discussion 1175.

19.    Demaurex, N. and S. Grinstein, *Na+/H+ antiport: modulation by ATP and role in cell volume regulation.* J Exp Biol, 1994. **196**: p. 389-404.

20.    Cameron, I.L., et al., *Intracellular concentration of sodium and other elements as related to mitogenesis and oncogenesis in vivo.* Cancer Res, 1980. **40**(5): p. 1493-500.

21.    Ouwerkerk, R., et al., *Tissue sodium concentration in human brain tumors as measured with 23Na MR imaging.* Radiology, 2003. **227**(2): p. 529-37.

22.    Reshkin, S.J., et al., *Na+/H+ exchanger-dependent intracellular alkalinization is an early event in malignant transformation and plays an essential role in the development of subsequent transformation-associated phenotypes.* FASEB J, 2000. **14**(14): p. 2185-97.

23.    Rotin, D., et al., *Requirement of the Na+/H+ exchanger for tumor growth.* Cancer Res, 1989. **49**(1): p. 205-11.

24.    Kometiani, P., L. Liu, and A. Askari, *Digitalis-induced signaling by Na+/K+-ATPase in human breast cancer cells.* Mol Pharmacol, 2005. **67**(3): p. 929-36.

25.    Ouwerkerk, R., et al., *Elevated tissue sodium concentration in malignant breast lesions detected with non-invasive 23Na MRI.* Breast Cancer Res Treat, 2007. **106**(2): p. 151-60.

26.    Bartha, R., J.F. Megyesi, and C.J. Watling, *Low-grade glioma: correlation of short echo time 1H-MR spectroscopy with 23Na MR imaging.* AJNR Am J Neuroradiol, 2008. **29**(3): p. 464-70.

27. Farag, A., et al., *Unshielded asymmetric transmit-only and endorectal receive-only radiofrequency coil for (23) Na MRI of the prostate at 3 tesla.* J Magn Reson Imaging, 2015. **42**(2): p. 436-45.

28. Ward, A.D., et al., *Prostate: registration of digital histopathologic images to in vivo MR images acquired by using endorectal receive coil.* Radiology, 2012. **263**(3): p. 856-64.

29. Axel, L., J. Costantini, and J. Listerud, *Intensity correction in surface-coil MR imaging.* AJR Am J Roentgenol, 1987. **148**(2): p. 418-20.

30. Gibson, E., et al., *Registration of prostate histology images to ex vivo MR images via strand-shaped fiducials.* J Magn Reson Imaging, 2012. **36**(6): p. 1402-12.

31. Gibson, E., *3D fusion of histology to multi-parametric MRI for prostate cancer imaging evaluation and lesion-targeted treatment planning*, in *Biomedical Engineering*. 2014, The University of Western Ontario.

32. Thomsen, F.B., et al., *Active surveillance for clinically localized prostate cancer--a systematic review.* J Surg Oncol, 2014. **109**(8): p. 830-5.

33. National Comprehensive Cancer, N., *Prostate cancer. NCCN clinical practice guidelines in oncology.* J Natl Compr Canc Netw, 2004. **2**(3): p. 224-48.

34. Kanthabalan, A., M. Emberton, and H.U. Ahmed, *Biopsy strategies for selecting patients for focal therapy for prostate cancer.* Curr Opin Urol, 2014. **24**(3): p. 209-17.

35. van den Bos, W., et al., *Focal therapy in prostate cancer: international multidisciplinary consensus on trial design.* Eur Urol, 2014. **65**(6): p. 1078-83.

36. Kasivisvanathan, V., M. Emberton, and H.U. Ahmed, *Focal therapy for prostate cancer: rationale and treatment opportunities.* Clin Oncol (R Coll Radiol), 2013. **25**(8): p. 461-73.

37. Chalasani, V., A.K. Williams, and J. Chin, *Contemporary results of focal therapy for prostate cancer using cryotherapy.* Panminerva Med, 2010. **52**(3): p. 217-22.

38. Bauman, G., et al., *Boosting imaging defined dominant prostatic tumors: a systematic review.* Radiother Oncol, 2013. **107**(3): p. 274-81.

39. Langer, D.L., et al., *Prostate tissue composition and MR measurements: investigating the relationships between ADC, T2, K(trans), v(e), and corresponding histologic features.* Radiology, 2010. **255**(2): p. 485-94.

40. Vander Heiden, M.G., L.C. Cantley, and C.B. Thompson, *Understanding the Warburg effect: the metabolic requirements of cell proliferation.* Science, 2009. **324**(5930): p. 1029-33.

41. Goetze, K., et al., *Lactate enhances motility of tumor cells and inhibits monocyte migration and cytokine release.* Int J Oncol, 2011. **39**(2): p. 453-63.

42. Kato, Y., et al., *Acidic extracellular microenvironment and cancer.* Cancer Cell Int, 2013. **13**(1): p. 89.

43. Langer, D.L., et al., *Intermixed normal tissue within prostate cancer: effect on MR imaging measurements of apparent diffusion coefficient and T2--sparse versus dense cancers.* Radiology, 2008. **249**(3): p. 900-8.

44. Gibbs, P., et al., *Correlation of ADC and T2 measurements with cell density in prostate cancer at 3.0 Tesla.* Invest Radiol, 2009. **44**(9): p. 572-6.

45. Nielles-Vallespin, S., et al., *3D radial projection technique with ultrashort echo times for sodium MRI: clinical applications in human brain and skeletal muscle.* Magn Reson Med, 2007. **57**(1): p. 74-81.

46. Boada, F.E., et al., *Fast three dimensional sodium imaging.* Magn Reson Med, 1997. **37**(5): p. 706-15.

47. Staroswiecki, E., et al., *In vivo sodium imaging of human patellar cartilage with a 3D cones sequence at 3 T and 7 T.* J Magn Reson Imaging, 2010. **32**(2): p. 446-51.

Chapter 3

# 3   Discussion, Future Work and Conclusions

Provided in this chapter will be an overall summary of this thesis work and some limitations of this research. Additionally, some future directions for research in this area will be explored, specifically: expanding the patient cohort, prostate cancer monitoring using other imaging modalities, and the feasibility of using sodium-MRI to image other disease models.

## 3.1  Discussion

### 3.1.1   Summary of Thesis Work

This thesis investigated the relationship between tissue sodium concentration (TSC) and prostate cancer aggression. In this work, TSC was assessed using sodium magnetic resonance imaging (sodium-MRI) and Gleason-graded whole-mount histopathology was used as the *ground truth* for prostate cancer aggression. In this thesis work, I began my contribution to the image analysis by registering all acquired imaging data using a previously validated registration pipeline [1]. An in-depth explanation of the step-by-step process used for this registration is provided in Appendix A-1. After registration, Gleason contours are overlaid onto imaging data; allowing for accurate comparison of cancer stage (Gleason grade) to all imaging data. This rigorous process ensured that a specific voxel signal intensity from mpMRI or sodium-MRI data could be correctly associated with a specific Gleason grade found on the histology sections. Figure

3-1 provides a visual depiction of this process, where areas of a particular Gleason score on a histopathology section are carefully identified (Gleason 4+3 is the Gleason score used in the Figure 3-1 example) as masks of a specific Gleason score. Then, accurate registration ensures that when this mask is overlaid onto the imaging data, we can extract regional voxel signal intensity and compare that to the Gleason score of that area.
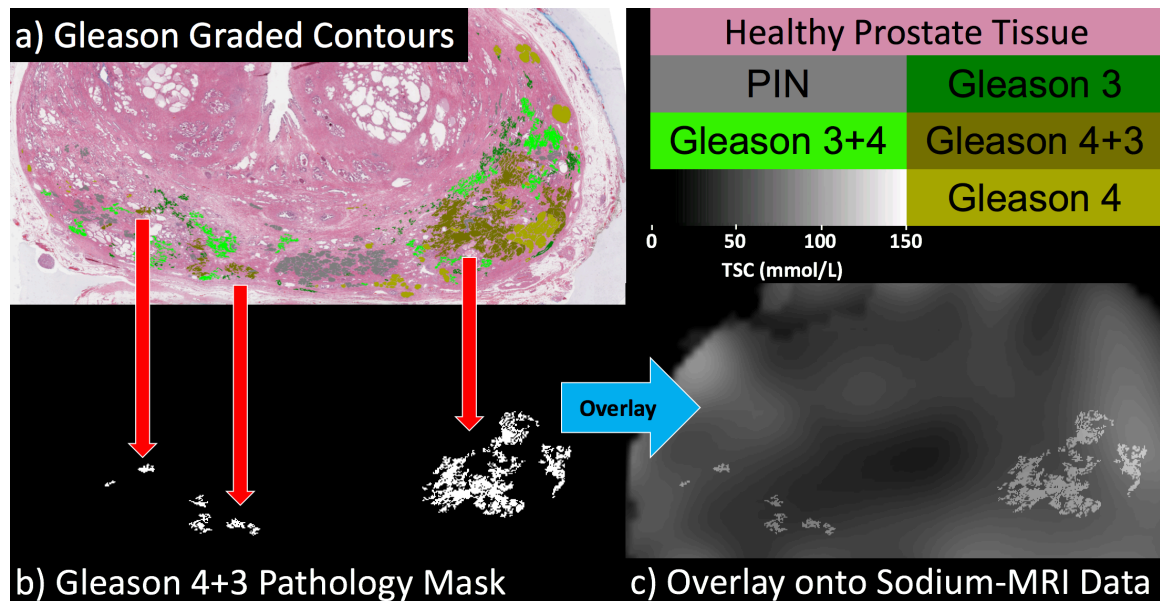


**Figure 3-1. Procedure for building pathology masks. Gleason contours (panel a) are used to build a pathology mask for one specific Gleason grade (panel b). In this illustration Gleason 4+3 is used. The red arrows indicate how the masks are built in the exact shape and size of the corresponding Gleason contour. These masks are then overlaid onto imaging data (panel c). In this illustration, TSC values acquired with sodium-MRI data is used. A Gleason grade legend and TSC signal intensity scale are shown in the top right panel.**

In this research, Gleason grade was compared to three sets of imaging data collected prior to each patient's prostatectomy surgery. These data were: apparent diffusion

coefficients (ADC) assessed by diffusion-weighted imaging, $T_2$-weighted images, and tissue sodium concentration measurements assessed by sodium-MRI. This work was the first-in-man study to compare and correlate the relationship between TSC and Gleason score. The sodium ion has many important functions in the body; it has been previously demonstrated to be a sensitive indicator of tumour cell motility and metabolism. Tumour metabolism, specifically the influence of the Warburg effect in cancerous tissue, leads to an increase in sodium ion concentration inside of the cell. Assuming a relatively constant extracellular tissue sodium concentration due to tissue perfusion [2], increases in TSC from normal tissue can then be hypothesized to be downstream effects of tumour cell metabolism. All sodium signal detected in this imaging was from endogenous sodium ions. In our study protocols, no sodium was administered to patients prior to imaging. However, as alluded to, many normal metabolic processes influence tissue sodium concentration levels in the body [3]. This highlights the potential for differences in baseline sodium levels between patients. If sodium-MRI is to be translated to clinical use, methods to account for the differences in sodium between patients must be considered. In this study, percent changes of TSC were assessed, allowing for regional assessment of changes in TSC associated with tumour grade in an individual patient. For this thesis, ΔTSC was used to denote the percent changes in tissue sodium concentration. The same percentage change method was used when analyzing $T_2$-weighted images, denoted as $\Delta T_2$. These calculations were done using Equation 2.1 (ΔTSC) and Equation 2.2 ($\Delta T_2$), described in Chapter 2, subsection 2.3.7. Imaging data in this thesis were collected across the whole prostate, sampling all zones of the gland. Data analysis was performed on the Gleason contours which were localized to the peripheral zone as research suggest that up to 80% of prostatic

cancers arise in this zone [4]. Additionally, proximity of the peripheral zone to the endorectal receive coil provided the highest SNR and lowest measurement uncertainties for the TSC analysis.

From our patient cohort of ten men, all with biopsy-proven prostate cancer, data were analyzed on an individual patient basis and then averaged together. TSC increases between Gleason grades in our data set were tested for statistical significance at the 0.05 level ($p<0.05$) using a one-way ANOVA and follow up Tukey test for all cases which had more than two Gleason grades available for comparisons ($n = 8$). Cases which had only two Gleason grades present on histology sections were tested for significance at the 0.05 level using an unpaired $t$-test ($n = 1$). Datasets where there were only one Gleason grade present are not included in individual patient statistical analysis ($n = 1$). The strength of the associations between whole patient cohort imaging data and Gleason grade were tested using a Spearman's non-parametric ranked correlation, producing the correlation coefficient, $r_s$. Sodium-MRI has shown promise as complementary imaging modality to mpMRI, which together would provide patients with a *non-invasive* imaging biopsy, able to localize *in vivo* cancer and then determine the cancer's aggression. Therefore, the clinical translatability of sodium-MRI as a useful assessment tool is grounded in its potential ability to characterize lesions on an individual patient basis. The results of this thesis work show that individual $\Delta$TSC values displayed an increasing trend with Gleason grade for all patients where more than one Gleason-scored lesion type was present ($n = 9$). Furthermore, feasible clinical translation requires the ability to differentiate between low- and high-risk prostate cancer, where the former is monitored with active surveillance and latter receives immediate intervention [5]. The widely accepted Gleason

grade distinction between these treatment options is between Gleason scores 3+4 and 4+3 [6]. Of the ten men analyzed, six possessed clinically significant, high-grade lesions ($\geq$ Gleason 4+3). Out of these six clinically significant cases, four displayed statistically significant increases across the threshold described above. These data have been graphed in Figure 2-8, within the Supplementary Figures section of Chapter 2. In total, six of the nine cases used for data analysis displayed statistically significant increases in $\Delta$TSC with Gleason grade, this is in addition to the increasing trend, which was observed in all $\Delta$TSC data sets. When averaged together, the patient cohort $\Delta$TSC data showed statistically significant increases between all grades ($p < 0.001$) (Figure 2-4). Additionally, patient cohort data possessed a significant correlation with Gleason grade ($r_s = 0.791$, $p < 0.01$).

The relationship between apparent diffusion coefficient (ADC) and Gleason grade has been previously examined and reported in the literature [7]. Reduced ADC values within tissue has been related to increased cellularity and membrane integrity. However, since ADC is not directly detecting metabolites which are inherently related to tumour metabolism, it is harder to assert that ADC values are unequivocally related to tumour aggression. This thesis work examined ADC values, measured by DWI, and compared them to histological Gleason scores. The results suggest that the association between ADC and tumour aggressiveness is not as robust as with TSC and lesion characterization using ADC data alone is not reliable for an individual patient. In this limited study, examination of ADC values from individual patients indicated a much weaker association with lesion grade (Figure 2-9). Some individual patient datasets possessed an inverse relationship between ADC values and increasing tumour grade (Patients 7, 8, 9, 10), a result seen in previous literature [7]; however, the majority of the cases possessed no overall trend ($n =$

5). Averaged patient cohort data (Figure 2-5) possessed similar results to the individual patients, as statistically significant differences were recorded between all grades ($p < 0.05$); however, this was not accompanied by any trend in the data, assessed by the Spearman's correlation ($r_s = -0.306$, $p = 0.079$).

Previous research has also looked at how quantitative $T_2$ contrast on $T_2$-weighted images, are related to prostate cancer. The results are mixed, with some research displaying no difference in $T_2$ values between cancerous and healthy tissue [8], while other studies show that highly dense cancers have reduced $T_2$ contrast in comparison to healthy tissue [9]. For characterizing lesions this can be problematic, as low signal intensity on $T_2$-weighted prostate images can also be attributed to non-cancerous prostatic conditions [8]. The data presented in this research from individual patients show that changes in $T_2$-signal intensity from healthy tissue ($\Delta T_2$) had very little correlation with Gleason score (Figure 2-10). Three of the nine cases possessed the expected inverse relationship of $\Delta T_2$ with Gleason grade. Statistical significance was seen in seven of the none cases, but only two were also accompanied by a decreasing trend. Averaged patient cohort data (Figure 2-6) displayed similar results to the individual data, with some statistical significance recorded ($p < 0.05$), but this was paired with an insignificant data trend ($r_s = -0.069$, $p = 0.699$).

In this thesis, we have highlighted the strong relationship between tissue sodium concentration measurements and histological Gleason grade. In this work, sodium-MRI was acquired in conjunction with mpMRI on men with biopsy-proven prostate cancer. These data were then accurately co-registered to Gleason-graded whole-mount histopathology. This allowed for direct comparison of imaging data to Gleason score. Imaging data included ADC values, $T_2$-weighted images, and TSC data. The sodium ion

has many important functions in tissue and has been previously demonstrated to be a sensitive indicator of tumour cell motility and metabolism. The work of this thesis was the first-in-man comparison and correlation of TSC values to Gleason grade. The results reported in this thesis work suggest that TSC assessed by sodium-MRI was more capable to distinguish between low- and high-grade prostate lesions than ADC measurements and $T_2$-weighted image contrast.

## 3.1.2 Limitations on Study Methodology

This research has several limitations. First, we assessed data from ten men, an $n$ value that is often considered to be small in a clinical setting. This was a difficult limitation to avoid, as men needed to first fall within the studies inclusion criteria. After selecting men who were candidates for the IGPC-2 study, they also needed to consent for sodium-MRI in addition to the standard protocols of the study. A total of seventeen men consented for sodium-MRI in addition to standard MRI. Of these seventeen men, four patients did not have high enough SNR to allow for accurate analysis, one withdrew due to a screen failure, one man did not return for prostatectomy surgery after imaging, and one patient showed no cancer in his prostate when the tissue went for Gleason grading. This left ten men who had successful imaging, prostatectomy surgery and subsequently tissue Gleason grading. Further, one of the ten datasets possessed only one Gleason grade (Gleason 3) on histology sections Therefore, analysis of imaging data changes between Gleason grades not possible. However, these data were included in patient cohort data analysis. An expanded cohort is planned after securing further funding to address this limitation (see section 3.2.1).

## 3.2  Future Work

### 3.2.1   Patient Cohort Expansion

This thesis work has presented the research from a pilot study, demonstrating that sodium-MRI has utility to be used in the clinic as complementary imaging data to multi-parametric-MRI. Together these techniques may be used as a *non-invasive* imaging biopsy, with high specificity to characterize *in vivo* prostate cancer grade. This information would be invaluable to clinicians and men with prostate cancer, as it has the potential to increase confidence in risk stratification decisions and to improve surveillance of low-risk disease. To facilitate this, these preliminary results need to be verified in a larger patient cohort with higher throughput. Future studies are planned, which will incorporate a dual-tuned ER receive coil, facilitating inherent registration of mpMRI and sodium-MRI data. This will eliminate a time-consuming co-registration step involving these data, as they will be obtained serially without changing RF coils (see Appendices A-1).

### 3.2.2   Additional Imaging Modalities for Prostate Cancer Detection

Sodium-MRI has been shown to be a sensitive indicator of prostate cancer grade, but additional imaging modalities can be useful to detect this disease, providing insight about the tumour tissue that is not evident through sodium-MRI. Dynamic-contrast enhanced MRI data can be collected in conjunction with other mpMRI contrasts. These data can be registered to Gleason graded histology using the same registration pipeline used in this thesis's research. Therefore, DCE-MRI wash-in, wash-out rates may be compared to Gleason score as further information for localization and characterization of

prostate cancer. Prostate-specific membrane antigen (PSMA) is a cellular surface protein whose expression increases 100-1000-fold in prostate cancer. This has made PSMA-ligands, which are radio-labeled to allow for detection using positron emission tomography (PET), a new sensitive tool for localizing prostate cancer. Additionally, labeled PSMA-PET ligands have been previously shown to have high sensitivity for prostate cancer cell metastases, an area of obvious clinical significance [10]. The superior anatomical delineable of multi-parametric-MRI has shown utility for locating suspicious regions in the human prostate [11]. Therefore, potential clinical workflow could involve mpMRI to locate potential lesions and sodium-MRI to characterize the lesion grade.

## 3.2.3    Using Sodium-MRI in Other Disease Models

Chapter 1-Section 1.3.2, described altered cellular metabolism within tumour cells involving upregulation of glycolysis (known as the Warburg Effect). This is not limited to prostate cancer and, as one might expect, increased TSC has also been observed in other cancers, including brain and breast cancer [12, 13]. Previous research has identified that the sodium-hydrogen antiporter (NHE1), one of the players responsible for increased sodium influx in tumour tissue, is ubiquitously expressed across cellular membranes of different tissue, including those within the breast and brain cells. In 2007, research by Ouwerkerk *et al.* showed that breast lesions significantly increased in tissue sodium concentration compared to unaffected tissue [13]. Additionally, research has suggested that the activity of NHE1 plays a role in the metastasis potential of breast cancer [14].  Brain cancer is a devastating diagnosis to patient, and approximately 1 in 123 Canadians will develop some form of brain cancer during their lifetime [15]. Glioma is the most common

form of primary brain cancer, accounting for roughly 80% of malignant brain tumours [16]. Previous studies have used sodium-MRI to quantify TSC in malignant brain tumours [12]. These results showed that sodium concentration in brain tumours were elevated compared to healthy brain tissue. Therefore, this highlights potential utility of using sodium-MRI assessed TSC to monitor tissue changes other tumour types such as breast and brain cancer.

## 3.3 Conclusions

Men diagnosed with prostate cancer are often faced with the stressful and uncertain decision about whether the best treatment of their cancer is active surveillance or radical treatment. Under diagnosis of prostate cancer is a concern due to the limited sample volumes obtained from prostate biopsy. This places a psychological burden on patients who have been diagnosed through biopsy with potentially less aggressive cancer because the widely-held belief is that cancer should be met head-on with curative treatment. Due to this, patients look to reject active surveillance protocols even if they are diagnosed with low-risk prostate cancer. These men instead opt for radical treatment, even if it may not be necessary for them. Accurate whole-gland lesion characterization tools can improve this situation. This research was undertaken to assess the relationship between data from magnetic resonance imaging contrasts and prostate cancer aggression. Imaging techniques are attractive solutions as they allow for whole-gland lesion assessment, creating a potential niche for *non-invasive* imaging assays. For this study, the "*ground truth*" for prostate cancer aggression was Gleason-graded whole-mount histopathology which was co-registered to imaging data. Imaging data collected included $T_2$-weighted imaging, diffusion-weighting imaging, and sodium-MRI. The results of this research show that endogenous tissue sodium concentration, assessed by sodium-MRI, was better than the mpMRI contrasts at unequivocally identifying the aggressiveness of prostate lesions. Furthermore, the combination of sodium-MRI with mpMRI could provide the basis for an imaging biopsy, providing accurate complementary information to patients related to their prostate cancer aggressiveness. This may be another small step along the path toward precision medicine.

# References for Chapter 3

1. Ward, A.D., et al., *Prostate: registration of digital histopathologic images to in vivo MR images acquired by using endorectal receive coil.* Radiology, 2012. **263**(3): p. 856-64.

2. Thulborn, K.R., et al., *Comprehensive MR imaging protocol for stroke management: tissue sodium concentration as a measure of tissue viability in nonhuman primate studies and in clinical studies.* Radiology, 1999. **213**(1): p. 156-66.

3. Titze, J., *Sodium balance is not just a renal affair.* Curr Opin Nephrol Hypertens, 2014. **23**(2): p. 101-5.

4. McNeal, J.E., et al., *Zonal distribution of prostatic adenocarcinoma. Correlation with histologic pattern and direction of spread.* Am J Surg Pathol, 1988. **12**(12): p. 897-906.

5. Mohler, J.L., et al., *Prostate Cancer, Version 1.2016.* J Natl Compr Canc Netw, 2016. **14**(1): p. 19-30.

6. Morash, C., et al., *Active surveillance for the management of localized prostate cancer: Guideline recommendations.* Can Urol Assoc J, 2015. **9**(5-6): p. 171-8.

7. Hambrock, T., et al., *Relationship between apparent diffusion coefficients at 3.0-T MR imaging and Gleason grade in peripheral zone prostate cancer.* Radiology, 2011. **259**(2): p. 453-61.

8. Hoeks, C.M., et al., *Prostate cancer: multiparametric MR imaging for detection, localization, and staging.* Radiology, 2011. **261**(1): p. 46-66.

9. Langer, D.L., et al., *Intermixed normal tissue within prostate cancer: effect on MR imaging measurements of apparent diffusion coefficient and T2--sparse versus dense cancers.* Radiology, 2008. **249**(3): p. 900-8.

10. van Leeuwen, P.J., et al., *Prospective evaluation of 68Gallium-prostate-specific membrane antigen positron emission tomography/computed tomography for preoperative lymph node staging in prostate cancer.* BJU Int, 2017. **119**(2): p. 209-215.

11. Kirkham, A.P., M. Emberton, and C. Allen, *How good is MRI at detecting and characterising cancer within the prostate?* Eur Urol, 2006. **50**(6): p. 1163-74; discussion 1175.

12. Ouwerkerk, R., et al., *Tissue sodium concentration in human brain tumors as measured with 23Na MR imaging.* Radiology, 2003. **227**(2): p. 529-37.

13. Ouwerkerk, R., et al., *Elevated tissue sodium concentration in malignant breast lesions detected with non-invasive 23Na MRI.* Breast Cancer Res Treat, 2007. **106**(2): p. 151-60.

14. Amith, S.R. and L. Fliegel, *Regulation of the Na+/H+ Exchanger (NHE1) in Breast Cancer Metastasis.* Cancer Res, 2013. **73**(4): p. 1259-64.

15. Statistics, C.C., *Statistics CCSAC on Cancer Statistics.* 2017.

16. Omuro, A. and L.M. DeAngelis, *Glioblastoma and other malignant gliomas: a clinical review.* JAMA, 2013. **310**(17): p. 1842-50.

# Appendices A-1: In-Depth Description of the Image Co-Registration Pipeline

An important aspect to success of the research presented in this thesis was the accurate co-registration of all imaging data to the whole-mount histopathology slices which were Gleason graded by a pathologist assistant and subsequently confirmed by an expert genitourinary pathologist. For this study and in the clinic, Gleason grading of tissue samples is the gold standard for assessment of prostate cancer aggression. Therefore, accurate registration is very important to ensure that the extracted imaging voxel signal intensity is correctly compared to that voxels pathological Gleason score. In this description, we will be referring to the imaging data shown in Figure 0-1, which has been adapted from a previously shown figure in Chapter 2 (Figure 2-1). These data include: *in vivo* high-resolution $T_2$-weighted images, *in vivo* low-resolution $T_2$-weighted images, *ex vivo* $T_1$ and $T_2$-weighted image sets, whole-mount digitized histopathology, *in vivo* sodium-MRI images.
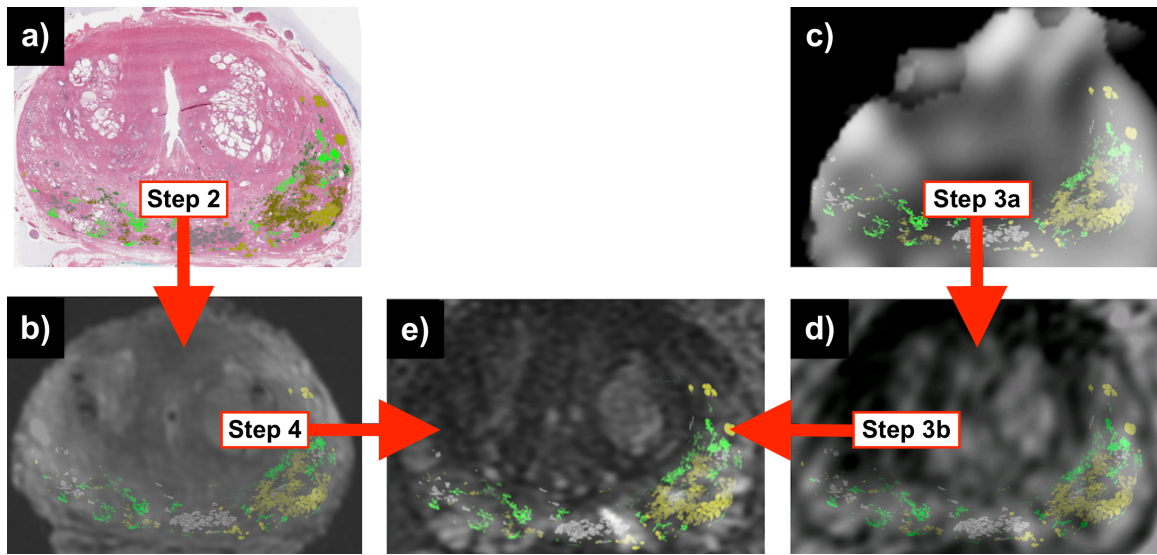
**Figure 0-1. The imaging volumes used in this study and their position along the registration pipeline. Step 1 (not shown) is preparation of the prostate specimens for high-resolution bright-field scanning and subsequent Gleason grading. Digitized whole-mount histopathology with Gleason graded lesions (panel a) are registered to the *ex vivo* $T_2$-weighted image (panel b) through the process described in Step 2. *In vivo* sodium-MRI data (panel c) are registered to the lower-resolution *In vivo* $T_2$-weighted volume (panel d) through the process described in Step 3a. The low-resolution *In vivo* $T_2$-weighted image set is registered to the high-resolution *In vivo* $T_2$-weighted image set (panel e) through the Step 3b's procedure. Finally, *ex vivo* $T_2$-weighted images are registered to high-resolution *In vivo* $T_2$-weighted images through the Step 4 procedure.**

## Step 1: Prostate Specimen Preparation

The image registration pipeline begins after radical prostatectomy, where excised prostates are fixed in formalin and laced with MRI-visible fiducial markers (3 internal and

7 external). These fiducial markers are designed to be soft to avoid tissue disruption [1]. This is because a pathologist's evaluation of the excised prostate tissue affects a patient's clinical outcomes, so these fiducials should not influence that. These prostate sections are then MR imaged *ex vivo*. After imaging, the prostate specimens are sliced into sections 4.4 mm apart [1]. This slicing is important to ensure that each cut is along the plane acquired during imaging or at least as nearly parallel as possible. This step was performed by collaborator Cathie Crukley.

## Step 2: Registration of *Ex Vivo* MR Images to Histology

After slicing, these histology sections are registered to the previously acquired $T_1$- and $T_2$-weighted *ex vivo* image set. Image registration was done on the $T_1$-weighted image, but the $T_2$-weighted images are acquired serially and are therefore registered inherently using the exact same fiducials. This step was performed by Dr. Aaron Ward's group, specifically Chapter 2 co-author Peter Martin.

## Step 3: Registration of *In Vivo* MR Image Sets

**Step 3a)** The registration between the low-resolution $T_2$-weighted image set and the sodium-MRI image sets was a rigid automatic registration. Both images were taken using the same endorectal (ER) receive radiofrequency (RF) coil in the same MR exam which facilitated this registration using fixed fiducial points which were enclosed in the reference vials used for calculation of absolute TSC values. The reference vials were situated within the ER probe itself, so applicator of a simple rotation allowed for registration of these image sets.

**Step 3b)** The deformable co-registration of the low-resolution $T_2$-weighted image set acquired with the rigid $^{23}$Na ER probe to the high-resolution $T_2$-weighted image set taken with an inflatable $^1$H ER probe. To perform this registration, approximately 10-15 preliminary fiducial points are placed on physiologically relevant regions of interest (ROI) that are identifiable on both imaging volumes. These ROI's include areas of hypo-intense signal such as benign prostatic hyperplasia and hyper-intense cystic spaces [1]. It is important these some of the preliminary fiducials are placed around the perimeter of the prostate, to allow for accurate overlay. Once the 10-15 homologous preliminary fiducial points are specified, the user selects both an input volume and a reference volume. The input volume will be deformed to the reference volume during registration. After this selection, the two image sets and associated fiducial points are plugged into a non-rigid, interactive thin-plate spline (TPS) extension [2] within the 3D Slicer software (Surgical Planning Laboratory, Harvard Medical School, Boston, MA, USA, Version 4.3.1). The TPS module deforms the input volumes to fit the reference volume based upon the specified fiducial points. After the rough registration of the two volumes using the 10-15 points, 35-40 more fiducial points are chosen on the images. As each new fiducial point is chosen, a real-time deformation of the input volume to the reference volume is performed. The registering scientist can delete old fiducial points that they decide are not necessary or are not as accurate as originally thought. On average, a full registration will have 50 fiducial points.

# Step 4: Registration of *Ex Vivo* and *In Vivo* MR Image Sets

The last step in this study's registration pipeline, is the co-registration of both the *ex vivo* imaging volumes ($T_1$- and $T_2$-weighted) with the high-resolution $T_2$-weighted image set. The $T_1$- and $T_2$-weighted image sets are automatically registered to each other, so we only needed to register the $T_2$-weighted image sets for full image registration. We use the $T_2$-weighted *ex vivo* images because registration requires comparison of ROI's which have homologous contrast enhancement with respect to surrounding tissue. The procedure for this non-rigid, deformable registration is the same as explained in Step 3. When the pipeline has been successfully completed, we expect an *in vivo* MRI to histopathology co-registration error of ~ 1.5 mm [1].

# References for Appendices A-1

1.      Ward, A.D., et al., *Prostate: registration of digital histopathologic images to in vivo MR images acquired by using endorectal receive coil.* Radiology, 2012. **263**(3): p. 856-64.

2.      Gibson, E., *3D fusion of histology to multi-parametric MRI for prostate cancer imaging evaluation and lesion-targeted treatment planning*, in *Biomedical Engineering*. 2014, The University of Western Ontario.

# Appendices A-2: Use of Human Participants – Ethics Approval Notice

**Use of Human Participants - Ethics Approval Notice**

*Research*

# Western

**Principal Investigator:** Dr. Joseph Chin
**Review Number:** 18135
**Review Level:** Full Board
**Approved Local Adult Participants:** 60
**Approved Local Minor Participants:** 0
**Protocol Title:** Multi-modality Prostate Cancer Image Guided Interventions
**Department & Institution:** Oncology,London Health Sciences Centre
**Sponsor:** Canadian Institutes of Health Research

**Ethics Approval Date:** September 08, 2011          **Expiry Date:** September 30, 2014

Documents Reviewed & Approved & Documents Received for Information:

| Document Name | Comments | Version Date |
|---|---|---|
| UWO Protocol | | |
| Letter of Information & Consent | | 2011/05/30 |
| Investigator Brochure | Version 1.0 - received for information only | 2011/04/19 |
| Protocol | Received for information only | 2011/05/30 |

This is to notify you that the University of Western Ontario Health Sciences Research Ethics Board (HSREB) which is organized and operates according to the Tri-Council Policy Statement: Ethical Conduct of Research Involving Humans and the Health Canada/ICH Good Clinical Practice Practices: Consolidated Guidelines; and the applicable laws and regulations of Ontario has reviewed and granted approval to the above referenced study on the approval date noted above. The membership of this HSREB also complies with the membership requirements for REB's as defined in Division 5 of the Food and Drug Regulations.

The ethics approval for this study shall remain valid until the expiry date noted above assuming timely and acceptable responses to the HSREB's periodic requests for surveillance and monitoring information. If you require an updated approval notice prior to that time you must request it using the UWO Updated Approval Request form.

Member of the HSREB that are named as investigators in research studies, or declare a conflict of interest, do not participate in discussions related to, nor vote on, such studies when they are presented to the HSREB.

The Chair of the HSREB is Dr. Joseph Gilbert. The UWO HSREB is registered with the U.S. Department of Health & Human Services under the IRB registration number IRB 00000940.

Ethics Officer to Contact for Further Information

*This is an official document. Please retain the original in your files.*

The University of Western Ontario
Office of Research Ethics
Support Services Building Room 5150 • London, Ontario • CANADA – N6G 1G9
PH: 519-661-3036 • F: 519-850-2466 • ethics@uwo.ca • www.uwo.ca/research/ethics

# Curriculum Vitae

| | |
|---|---|
| **Name:** | Nolan Christopher Broeke |

**Post-secondary Education and Degrees:**

**Master's of Science**
Medical Biophysics (Molecular Imaging)
University of Western Ontario
London, Ontario, Canada
September 2016 – June 2018

**Bachelor of Science**
Honors (Major in Life Sciences)
Queens University
Kingston, Ontario, Canada
September 2012 – April 2016

**Honours and Awards:**

**Western Graduate Research Scholarship**
Department of Medical Biophysics. University of Western Ontario
2016-2018

**Robarts Research Day Trainee Award (M.Sc. Student)**
Awarded for Oral Presentation at the Conference Proceedings
June 19, 2017

**Cellular and Molecular Imaging Symposium Poster Award**
Awarded for Poster Presentation and Conference Proceedings
May 1, 2018

**Publications:**

**NC Broeke**, J Peterson, J Lee, P Martin, A Farag, JA Lemus, M Moussa, M Gaed, J Chin, SE Pautler, A Ward, G Bauman, R Bartha, TJ Scholl. Characterization of Clinical Human Prostate Cancer Lesions Using 3.0-T Sodium-MRI Registered to Gleason-Graded Whole-Mount Histopathology. Under review at the *Journal of Magnetic Resonance Imaging*.